IN-SITU MONITORING OF MAGNETICALLY AUGMENTED ADDITIVE MANUFACTURING

An Undergraduate Research Scholars Thesis

by

RONALD SELLERS [1], CHRISTOPHER MCCULLOUGH [2], EDUARDO GONZALEZ [3], AND ADAM LIGHT [4]

Submitted to the LAUNCH: Undergraduate Research office at
Texas A&M University
in partial fulfillment of the requirements for the designation as an

UNDERGRADUATE RESEARCH SCHOLAR

Approved by
Faculty Research Advisors: Dr. Sarah J. Wolff
Dr. Hui Wang

May 2022

Majors: Industrial and Systems Engineering[1]
Aerospace Engineering[2, 3]
Materials Science and Engineering[4]

RESEARCH COMPLIANCE CERTIFICATION

Research activities involving the use of human subjects, vertebrate animals, and/or biohazards must be reviewed and approved by the appropriate Texas A&M University regulatory research committee (i.e., IRB, IACUC, IBC) before the activity can commence. This requirement applies to activities conducted at Texas A&M and to activities conducted at non-Texas A&M facilities or institutions. In both cases, students are responsible for working with the relevant Texas A&M research compliance program to ensure and document that all Texas A&M compliance obligations are met before the study begins.

We, Ronald Sellers[1], Eduardo Gonzalez[2], Christopher McCullough[3], and Adam Light[4], certify that all research compliance requirements related to this Undergraduate Research Scholars thesis have been addressed with our Research Faculty Advisors prior to the collection of any data used in this final thesis submission.

This project did not require approval from the Texas A&M University Research Compliance & Biosafety office.

TABLE OF CONTENTS

LIST OF FIGURES

ABSTRACT

In-Situ Monitoring of Magnetically Augmented Additive Manufacturing

Ronald Sellers[1], Christopher McCullough[2], Eduardo Gonzalez[3], and Adam Light[4]
Department of Industrial and Systems Engineering[1]
Department of Aerospace Engineering[2, 3]
Department of Materials Science and Engineering[4]
Texas A&M University

Research Faculty Advisor: Dr. Sarah J. Wolff
Department of Industrial and Systems Engineering
Texas A&M University

Research Staff Advisor: Dr. Hui Wang
Department of Industrial and Systems Engineering
Texas A&M University

Through advancements in technology over the last several years, additive manufacturing has become increasingly mainstream in the manufacturing process. Additive manufacturing has several traits which would theoretically make it superior to traditional subtractive manufacturing techniques. Additive techniques allow for fabrication of increasingly complex parts while maintaining design flexibility, reducing waste, and limiting costs. While this ability to manufacture complex parts is certainly applicable to the external structure, additive manufacturing will allow for control over the internal structure of a part as well. From this, porous components can be created which match desired mechanical properties somewhat independently of the material actually used for manufacturing. However, many of these advancements require further refinement of the additive manufacturing processes intrinsic to them. One of the techniques suggested as a method of improving additive manufacturing processes is the incorporation of magnets into the manufac-

turing process. These magnets are used to direct the flow of the melted metal with more precision. Experiments were conducted in order to evaluate the effects of the introduction of magnets on parts printed using Laser Powder Bed Fusion. Stainless steel 316L, a relatively cheap and easy to print steel, was printed onto a Ti64 substrate using both spot welding and line scanning. It was observed that magnets had an effect on the melt pool and the keyhole depth through and analysis of the spot welding. Additionally, the various magnets also changed the flow of particles in the melted areas generated through line scanning. While quantifying the magnetic fields' effects will require additional research and time, there is strong evidence that they could be a viable solution to increasing additive manufacturing's precision. While magnets are being explored as a way to augment current additive methods, certain parts of the basic process also benefit from further refinement. These aspects include the focal distance, dwell time, and power of the laser. In order to explore these variables, direct energy deposition was used in a modified form of spot welding. The printed SS316L showed that increased laser power or dwell time created a non-ideal ring of material around the print area. Additionally, an attempt to print hydroxyapatite ceramic on Ti64 was made to test for validity of future experimentation involving the two materials. From this it was clear that major issues arose when endeavoring to print a material with a higher melting point than the substrate. From these results the various processes intrinsic to additive manufacturing can be further refined.

DEDICATION

To our families, instructors, and friends who supported us throughout the research process. We thank you all for the guidance and encouragement.

ACKNOWLEDGMENTS

Contributors

The authors would like to thank our faculty advisor, Dr. Sarah Wolff, and our secondary advisor, Dr. Hui Wang, for their guidance and support throughout the course of this research. The authors would also like to acknowledge Samuel Clark, Kamel Fezzaa, and Alex Deriy at the beamline facility at Argonne National Laboratory.

We would like to acknowledge the Materials Characterization Facility (MCF) for allowing us to use their SEM/EDS machine for our experiments.

The materials analyzed/used for In-Situ Monitoring of Magnetically Augmented Additive Manufacturing were provided by Sarah Wolff, supplied by McMaster-Carr and Sigma Aldrich. Certain data and analyses depicted in In-Situ Monitoring of Magnetically Augmented Additive Manufacturing were conducted in part by Ronald Sellers, Christopher McCullough, and Marwan Haddad at Texas AM University in the department of Industrial and Systems Engineering.

All other work conducted for the thesis was completed by the student independently.

Funding Sources

Undergraduate research was supported by Sarah Wolff at Texas A&M University.

This research used resources of the Advanced Photon Source, a U.S. Department of Energy (DOE) Office of Science User Facility operated for the DOE Office of Science by Argonne National Laboratory (ANL) under Contract No. DE-AC02-06CH11357 and support through Laboratory Directed Research and Development (LDRD) funding from ANL under the same contract.

NOMENCLATURE

ANL	Argonne National Laboratory
AM	Additive Manufacturing
DED	Directed Energy Deposition
LPBF	Laser Powder Bed Fusion
Ti64	Ti-6Al-4V
AISI	American Iron and Steel Institute
SS316L	Stainless Steel 316L
HAp	Hydroxyapatite
$\frac{\partial \sigma}{\partial T}$	Surface tension
T	Temperature
Ma	Marangoni Flow number

1. INTRODUCTION

Interest in additive manufacturing (AM) has been on the rise in the last few years due to the Internet of things (IoT) and Industry 4.0. AM is a process of adding material in a layer-by-layer fashion in the 3D space. Industry 4.0, otherwise known as the fourth industrial revolution, is the ongoing automation of traditional machining and manufacturing. This is achieved with cloud computing, robot-oriented machining, artificial intelligence (A.I.), and smart diagnostics to observe processes and make changes real-time in the manufacturing industry. Industry 4.0 encompasses the use of AM techniques, such as 3D printing, laser powder bed fusion (LPBF), directed energy deposition (DED), selective laser melting (SLM), and others. This has led to the advancement of using AM and titanium alloys in various industries from aerospace, biomedical, dental, and even nuclear [1]. Future work would involve looking at external process parameters, such as using magnetic fields, vibration waves, and other types of noise that could change the AM process.

1.1 Problem Definition

Additive manufacturing is great for rapid prototyping and the fabrication of complex parts, however there are some issues that arise with the process. These issues include porosity, grain boundary alignment, mechanical properties, melt pool formation, and various others [2, 3, 4, 5, 6, 7, 8, 9, 10]. Many of these issues arise from the process parameters of the experiment such as laser power, scan speed, powder deposition rate, and shielding gas pulse rate. Another issue this field faces is the difference in materials. Not every material has the same melting point or specific heat, meaning it will be harder or easier to combine depending on if it is a ceramic or metal. Certain questions are asked if there are any other parameters that can be changed, internal or external, and what sort of impact do those parameters have on the final part. This study will attempt to understand how to control the additive manufacturing process by using magnetic fields to improve part formation and to reduce unwanted defects within different material printing.

1.2 Background

Previous studies have been done on topics involving DED/LPBF, Ti64, HAp, and SS316L to try and understand the behavior of these materials and how the process parameters affect the final product. One of the studies observed the development of a composite of Ti64 with silicon and HAp for load-bearing implants. *Bandyopadhyay et. al.* found that titanium and vanadium silicides were formed after the introduction of Si, increasing the hardness by 114%, decreasing the coefficient of friction and wear rate by 38.1% and 70.8% , respectively [11]. Multiple studies have been conducted on laser deposited Ti64 to look at anisotropy, microstructure, tensile strength, hardness, and various other mechanical properties [12, 13, 14]. These experiments deal with Ti64 deposition, however in this study the Ti64 is used as the substrate with a foreign powder deposited. It is important to have the previous studies to perform a comparative analysis to understand what is changing and how the process is affected.

Process parameters play a key role in the chemical and physical combination of metals for AM techniques. Some of the previous studies done have analyzed different process parameters for combining HAp and Ti64 together [11, 15]. *Zhang et. al.* and *Beese et. al.* found yield and tensile strength decreased with increasing laser power and decreased scanning speed [16, 17]. The laser power ranged from 600 W to 1400 W while the scanning speeds ranged from 2 mm/s to 10 mm/s. The microstructure and phases of the SS 316L composites were analyzed using a scanning electron microscope (SEM) and x-ray diffraction (XRD). They had found that microstructure of the deposited SS316L was composed of slender dendrites that grew out epitaxilly from the substrate [16]. A study done by *Beese et. al.* observed the parameters for working with AISI 304L stainless steel on a DED process. This study looked at the microstucture and anisotropy of the AISI 304L steel when printing wall like structures with linear heat inputs of 271 and 377 J/mm [17]. They found that yield strength, ultimate tensile strength, and ductility were higher in the lower linear heat input. Along with this, the ductility was less in the longitudinal direction than the transverse direction [17]. Like the previous study with anisotropy, *Wolff et. al.* observed how process parameters affect the anisotropy of Ti-6Al-4V alloy. Using various models, equations, and changing

certain process parameters, one of the conclusions drawn from their study was that the J-factor can be used to observe the linkage between porosity and process parameters [12]. They also found that with increasing laser power up to around 940 W caused an increase in elongation and strength of the part. Observations such as these are important in understanding what others have done and how to improve this study to be efficient and to be able to show similar or different results.

Magnetic fields can be used within the additive manufacturing process to alter in-situ dynamics like melt pool and porosity formation that in turn change final product structure as well as the. Different forces act within the vector fields created by magnetic and electric induced fields within the additive manufacturing processes, such as curie temperature and Lorentz Forces. Curie temperature of a material is the temperature at which materials lose their permanent magnetic properties [18, 19]. Lorentz forces are electric and magnetic forces acting on a point charge due to the electromagnetic fields. Curie temperatures and Lorentz forces can still impact the additive manufacturing process even when the materials used are not naturally ferromagnetic. Previous studies have been conducted to observe such phenomena, such as subjecting the part to a solenoid magnet, a spinning electromagnet, and various others during the process [20, 21, 22]. Altering the grain boundary changes the texture of the material on the final product, proving to be useful in different applications such as automotive or biomedical. *Wang et. al.* found that the <110> grain boundary of an Inconel 718 super-alloy typically aligned with a transverse magnetic field, which showed that the average grain boundary misorientation angle decreased from 32° to around 19° [22]. Moreover, they proved how magnetic fields favored controllable textures and impacted the grain morphology and elemental distribution. Another study done by *Smith et. al.* involved using a programmable solenoid to induce a dynamically changing magnetic field around the DED experiment [23]. The study focused on the parameters of the DED experiment in order to enhance the mechanical properties. They found that inducing a magnetic field improves the material efficiency by 25% and how a fixed solenoid in a specific location increased the cross-sectional area of the tracks by up to 83%.

1.3 Motivation

The motivation behind this study is to understand how to change the additive manufacturing process to better fabricate parts, as well as perform a validity study using different materials. Not all metals or composites used in additive manufacturing, specifically DED, are magnetic. We plan to implement induced magnetic fields within the manufacturing process. Understanding how magnetic fields can affect non-magnetic materials is an important objective that this paper aims to accomplish. Using the previous work done as a guide, this study will observe the effect of magnetic fields on the material by looking at certain phenomena such as porosity, key-hole formation, melt pool width, and particle flow within molten fluid.

1.4 Summary

The work done here is important in understanding how to alter the experiment parameters and induce magnetic fields in order to create the desired part. It focuses on microstructure and melt pool characteristics of the newly formed parts using varying process parameters. Future work can be done with magnetic fields that deal with changing the strength of the field, angle of the magnets, and overall design and implementation of the magnets into the experiment. We will observe how certain characteristics such as keyhole depth, melt pool width, melt flow dynamics, and composition change with magnetically augmented LPBF experiments.

This paper also aims to observe the viability of printing SS316L and HAp on Ti64 within a custom-built DED machine. We will look at binding capabilities between materials with certain chemical compositions and if this process is possible for future work with these materials and methods.

2. METHODS

2.1 Printing Methods

There are two types of deposition devices used throughout our experimentation. The first is a laser powder bed fusion (LPBF). A few of the results analyzed with SEM and x-ray analysis came from experiments done at Argonne National Laboratory (ANL) using LPBF techniques with Ti64 substrate, Stainless Steel 316L (SS316L) powder, and magnetic fields in the process. The magnets used at ANL were positioned on the cross-section of the metal to induce a magnetic field parallel with the laser during line scanning and spot welding experiments, which can be visualized in **Figure 2.1**. The other experiments conducted and analyzed used a custom built DED machine by Dr. Sarah Wolff at Texas A&M University. These experiments used Ti64, SS316L, and hydroxyapatite (HAp).

The experiments were re-simulated in software to visualize the magnetic field vectors. This is helpful to understand how the magnets affect the substrate that sits in-between the magnets, in a sandwich-like structure. Experiments were simulated in the open source software Finite element method magnetics (FEMM), as well as in the ANSYS Mechanical magneto-static simulation. Values were not taken from these simulations, however their non-linear magnetic B-H curves are within accordance to the manufacturer and supplier standards. The magnetic flux density fields can be seen in **Figure 2.1**.

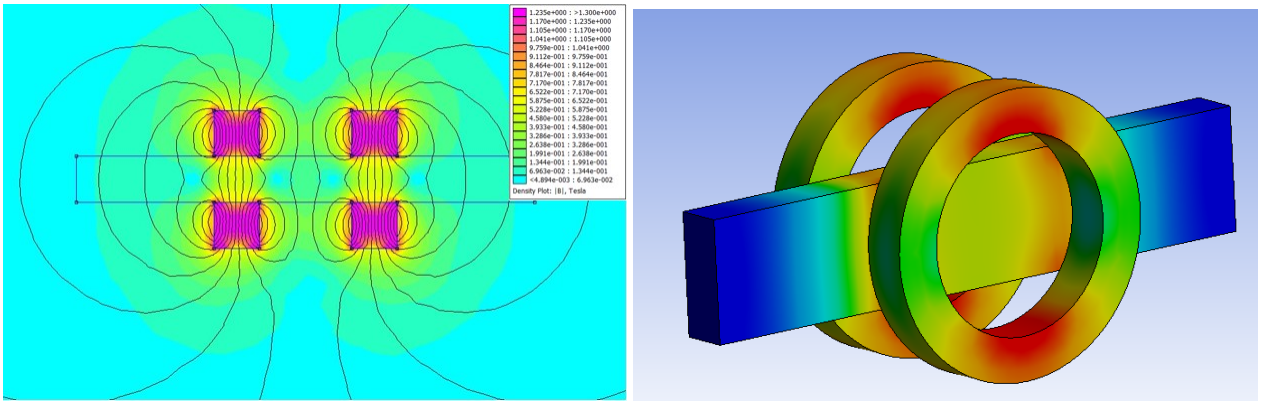

(a) FEMM (b) ANSYS Model

Figure 2.1: a) Cross-section magnetic field simulation using FEMM; b) ANSYS Mechanical Mangeto-static model; Both models used numerical values provided by the supplier, K&J Magnetics

2.1.1 Laser Powder Bed Fusion

Laser powder bed fusion is presently the most common method of additively manufacturing parts. This process involves placing the printing powders in layers in the "bed" and then melting them with a laser [24]. This technique is popular as it reduces the total number of variables associated with printing when compared to a more complicated process like DED. Another advantage is the ability to import models directly from computer-aided design (CAD) files. The LBPF technique then slices this three-dimensional model into two-dimensional layers for the printing. This gives the manufacturer control over the thickness of each layer enabling the creation of highly complex structures. Parts fabricated have been proven to have a shorter manufacturing time and be cheaper compared to processes like molding [24].

2.1.1.1 Spot Welding

Spot welding is the simplest type of additive manufacturing printing and involves holding the laser over a set point for a short period, known as dwell time. While this type of printing has limited practical value, it does allow for a greater degree of observation of critical print characteristics such as the geometry of the area melted by the laser, porosity formation, and powder spread

behavior. Additionally, due to its simplicity, a significant number of spot welded experiments can be conducted in a short amount of time increasing the validity of results.

2.1.1.2 Line Scanning

Line scanning is a type of printing wherein the laser moves over a set length in a single direction, melting powder as it goes. An analysis of this type of printing can be used to show the affects on the material as the laser moves across it. These affects include the pores left after melting and how particles move throughout the fluid. This sort of analysis is especially important for LPBF where the printing is done in layers as the properties of preceding layers have significant effects on the following ones. The setup for the LBPF experiments can be seen in **Figure 2.2**.

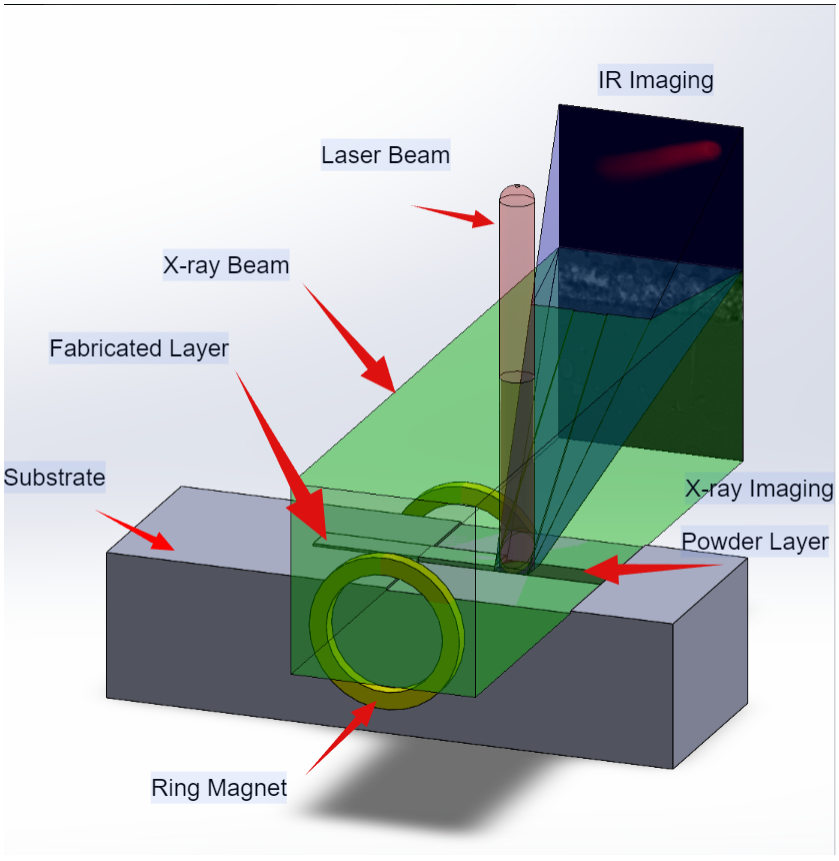

Figure 2.2: Setup for LPBF printing and imaging

2.1.2 Directed Energy Deposition Machine

A custom DED machine was designed and built by Dr. Sarah Wolff, which is seen in **Figure 2.3**. This machine utilizes 3 ft^3 of space for the chamber, with a capable printing size of 100 mm^3 for the movement of the motors in the xyz planes. The laser in use is an IPG Fiber Laser with a maximum power of 440W, mounted directly above the base plate. This DED machine utilizes a four-flow powder deposition technique that allows for powder to be dispensed evenly around the laser. Inert gas is needed in most DED cases, in which Argon gas is used as the experiment shielding gas.

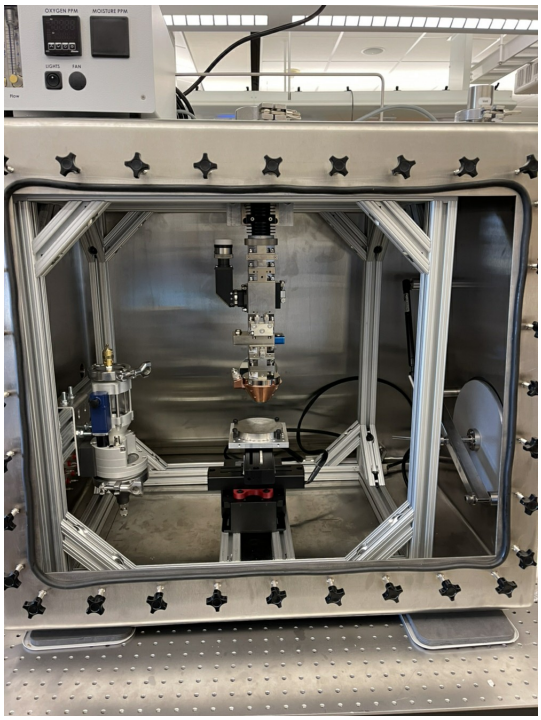

Figure 2.3: DED machine inside the lab with the laser mounted directly above the xyz motors with a powder hopper directly to the left of the base plate

2.2 Materials

Three materials are used within the experimentation, which are Ti64, SS316L, and HAp. Each material was chosen due to their respective strengths, biocompatbility, printibility, and overall

cost effectiveness for fabricated parts. The materials and their respective characteristics can be found below in **Table 2.1**:

Table 2.1: Material Listing and Respective Properties

Material	**Powder Size**	**Composition**	**Purpose**
Ti-6Al-4V	N/A	$Ti-6Al-4V$	Substrate
Stainless Steel 316L	45 μm	$FeCr_{18}Ni_{10}Mo_3$	Substrate/Powder
Hydroxyapatite	10 μm	$Ca5HO13P3$	Powder

2.2.1 Ti-6Al-4V

Ti-6Al-4V (Ti64) is a titanium alloy that is already widely used for biomedical applications. The Ti64 was used as a substrate in these experiments and was supplied by McMaster-Carr as Grade 5 titanium bars and meets the ASTM B265 specifications. It is primarily composed of titanium, aluminum, and vanadium with trace amounts of other metals. Ti64 has a high specific strength and low electrical conductivity, both of which are traits that lend themselves toward high bio-compatibility [25, 26, 27]. For these reasons Ti64 is used for a variety of implants which replace hard tissue. Some examples of applications are artificial knee joints, bone plates, and artificial hip joints [28].

By using Ti64 as a base with other material printed upon it, some of the shortcomings of the alloy can be removed. Ti64 has low wear resistance properties [29], which can lead to undesirable fatigue in implants that experience a large number of cycles, such as hip replacements. Additionally, Ti64 has a significantly higher elastic modulus than that of bone. This can lead to higher stress concentrations on the bones associated with the implant than the skeletal structure experienced originally [30]. Additive manufacturing techniques can help to alleviate both of these issues by exerting a greater amount of precision on the manufacturing process. By using Additive Layer Manufacturing (ALM) the structure of the Ti64 can be made more porous and therefore,

have a elastic modulus very close to that of bone [31]. Additive manufacturing can also be used to reduce the wear resistance issue by printing a layer of a more ideal material on top of the Ti64. By using this method, manufacturers can achieve an implant with both the material proprieties of the Ti64, and the superior surface properties of the coating.

2.2.2 Stainless Steel 316L

Stainless Steel 316L (SS316) is one of the most commonly used metals for implants due to biocompatibility [32, 33, 34, 35]. The AISI 316L used in the experiments had a chemical composition of $FeCr_{18}Ni_{10}Mo_3$. SS316L is known to have great mechanical properties as well, such as high tensile strength, elastic modulus, and great corrosion resistant properties. One of the other great reasons for using SS316L is that it is relatively cheap compared to another biocompatible metal used in implants such as cobalt chromium (CoCr). Since SS316L is more dense than bone and has higher elastic modulus, this can lead to stress shielding. Stress shielding is the reduction of bone caused by loss of stress on the bone from the implant. To combat this, SS316L is typically coated with other materials such as Ti64 or hydroxyapatite [34]. However, not every SS316L implant of medical device that resides within the human body needs to be coated.

For some medical applications, *Dewidar et. al.* found that porous SS316L was more suitable. In fact, they found that the elastic modulus ranged between 26 to 43 GPa while the compressive strength ranged from 21 to 32 MPa [35]. In their study, they used selective laser sintering (SLS) to fabricate the SS316L parts and found that the porosity was between 40% and 50%. Finally, they observed the steel with a porosity around 50% typically displayed similar properties of compression and elastic modulus with that of human cortical bone [35]. Porosity is important when designing prosthesis since the lack of material in the part can make it lighter and therefore easier for the patient to wear.

2.2.3 Hydroxyapatite

Hydroxyapatite (HAp) is a bone-like ceramic with a chemical makeup denoted by the repeating unit, $Ca_{10}(PO_4)_6(OH)_2$. The HAp used in the experiments had a chemical formula of

$Ca5HO13P3$ with a density of 3.140 g/cm^3 and a molecular weight of 502.31 g/mol. This material is extremely close to that of human bone and is commonly used for alternatives in prosthesis and other medical devices/implants. HAp is a bioactive material, meaning it produces an effect on living tissue while promoting integration and bonding with surrounding bone. This leads to osteoinductive, which is stimulating differentiation of multi-potent cells into bone-forming lineages.

One of the most important factors in implant material is biointegration. Previous studies have been done on the comparison between Ti64 and HAp to determine their respective performance as implants. Some previous studies done on animals found that HAp implants observed biointegration within 4 weeks [36, 37]. *Block et. al.* also observed that 90% of the coated implants had a continuous layer of lamellar bone that connected the trabecular bone with the implant after 10 months of implementation, whereas in contrast, 50% of the Ti64 implants were coated after 10 months [36, 38]. These are some of the reasons are why the HAp is used as a coating on the metals and not mixed within material.

HAp is used in these experiments to test for viability to print with to see if it is an option to coat or mix with Ti64 through a specific type of manufacturing. Certain process parameters will be altered to find the key conditions to print and mix with, such as focal distance, dwell time, powder layer thickness, and laser power.

2.2.4 Magnets

The experiments consisted of long, short, and ring shaped N52 grade magnets. These magnets were supplied with manufacturer standards and certifications by K&J Magnetics, inc.

2.3 Image Analysis

One of the main methods of characterization performed was done using x-ray and thermal analysis. The experiments performed at Argonne National Labs involved high-powered X-Ray and thermal imaging cameras. X-ray images were captured at a recording rate of 40,000 and 50,000 frames per second, depending on experiment, while the number of frames captured was experiment dependent as well. Infrared (IR) images were captured at a rate of 20,000 frames per second. X-

ray images were used to measure different characteristics such as keyhole depth, melt pool width, porosity, and flow patterns of the material. IR images were used to observe different measures such as cooling rate and surface temperature plotting.

2.3.1 X-Ray Capturing and Measurements

The x-ray camera captures images that need to be processed in order to perform various analyses on. The software ImageJ was used to do this, which is a free and open source image processing program that can be used to draw, edit, and perform measurements on pictures/x-ray images [39, 40]. **Figure 2.4** represents the raw x-ray image captured by the camera on the left, while the image on the right shows the same image from experiment 173, but processed with ImageJ using image division and annotated in Microsoft VISIO. Certain aforementioned characteristics can be visually identified within the image shown. ImageJ can also be used to measure distances using the line function within the application. This was utilized to find the depth and width of the melt pool, however due to the x-ray camera recording ratio each measurement must be converted from pixels to μm by multiplying the values by a 1.97 ratio.

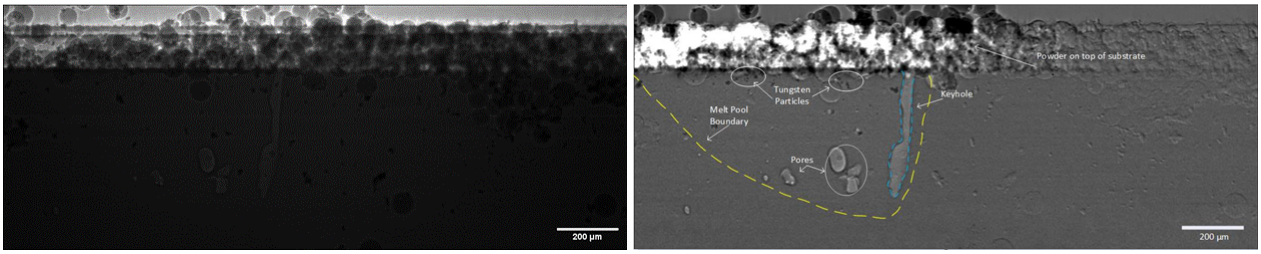

(a) Unprocessed (b) Processed and Annotated

Figure 2.4: a) Pre-processed x-ray image, directly from the camera; b) processed and annotated x-ray image to show experiment characteristics; X-ray image number 187/451 of experiment 173, involving SS316L, 43% Laser power, and a scan speed of 500 mm/s

2.3.1.1 Melt Pool Geometry

While there are a great deal of melt pool characteristics that are relevant to additive manufacture, two of the most important are the depth of the melt pool, which is referred to as the keyhole depth, and the melt pool width. The keyhole depth is relevant to the distribution of porosity throughout the print as well as the number of layers of powder the melt pool can reach. Without an understanding of the keyhole depth, manufactures can unintentionally melt areas of powder multiple times or not reach areas of powder at all. Though line scanning is more complex in terms of defining keyhole depth and melt pool boundary, a visualization of these characteristics are clearly visible in **Figure 2.4**. Melt pool width refers to the distance across the area melted by the laser. The width of this melt pool is relevant to several factors, but especially to the number of passes needed over a certain area of powder. A larger melt pool will mean a quicker print, but may also cause inconsistencies in the degree of particles melted throughout the flow.

2.3.2 Infrared Image Analysis

IR cameras capture the images in the form of a HTC file, which is a compressed file that holds the images. MATLAB is used to read this header, which then converts the HTC into TIFF images. Depending on the aspect ratio of the camera, TIFF images can be a wide range of sizes, but in this case they are 60x128 matrices. Each data point entry in the matrix is a temperature recorded by the camera. These images can then be re-read by MATLAB and transformed into the IR video recorded, which can be seen in **Figure 2.5**. This figure shows the evolution of the melt pool and temperature gradient over a few time intervals. IR videos are used to visualize the top-down view of the melt pool. These videos also allow for the extraction of certain characteristics such as temperature gradients and cooling rates.

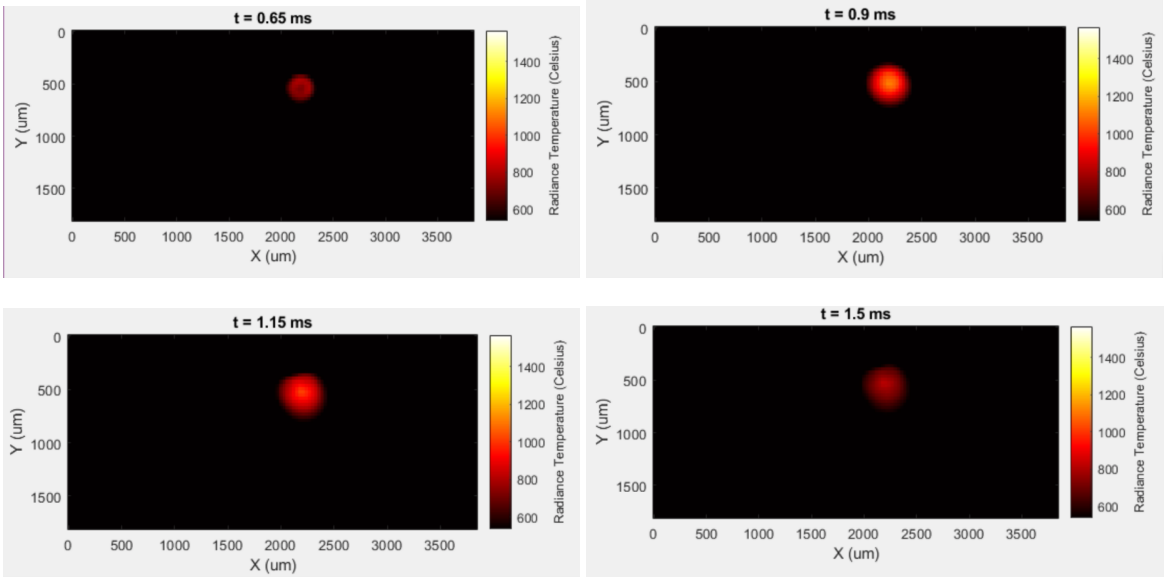

Figure 2.5: IR images of experiment 11, captured at different times (ms) to visualize the melt pool evolution and temperature gradient

2.4 Testing Method

2.4.1 Microstructure

A pre-polished sample can be seen in **Figure 2.6**. Microstructure is important in the analysis due to ISO 20160, which states that a homogeneous and stable microstructure are needed for biomaterial stability and integrity [41]. Before the samples could be viewed under a scanning electron microscope, they needed to undergo a few rounds of polishing, which is not necessary, but allows for better visualization.

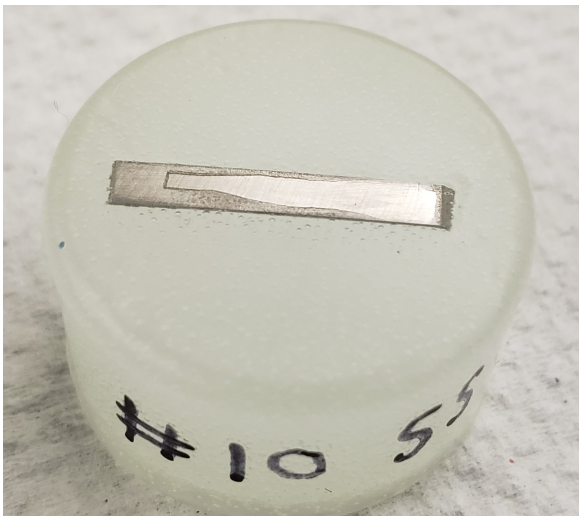

Figure 2.6: Pre-polished Sample of Stainless Steel subjected to a magnetic field during fusion

The machine that is used to study microstructure is the Scanning Electron Microscope (SEM). The SEM works by firing electrons through several condenser lenses to focus the beam so that the beam has a diameter on the nanometer scale. This beam then scans the surface of the sample. As the beam scans, the electrons are reflected off of the sample in different directions and picked up by a detector to display the image on screen. This image gives information relating to the surface of the material, and also allows features like grain boundaries, porosity, and surface finish to be observed. The contrast of the image is what will give information about the surface of the sample. Electrons that are reflected from surfaces not facing the detector will appear darker than those that do face the detector [42].

Prior to using the SEM, all surface contaminants need to be removed. This step is not necessary, but it helps in providing clearer images from the SEM. To do this, samples go through a polishing process that ends in an almost mirror surface finish. This process involves mounting the sample in a two-part resin and using a polishing machine with various grits of sandpaper. When polishing, it is important that both the sample surface and the epoxy side of the mount are level so that the sample surface is flat in the SEM. This step is crucial as a the electrons must bounce off of the level surface for accurate results. The first phase of polishing used a P4000 grit sandpaper on an

automatic polishing device. The final step to polishing is to use a cloth-like pad and a nanoparticle polishing compound to produce the mirror-like finish.

2.4.2 Energy Dispersive X-ray Spectroscopy

Energy dispersive spectroscopy (EDS) is a technique that can be used in tandem with the SEM machine. EDS works by firing electrons at the material and recording the x-rays that are emitted. Unlike x-ray photoelecton spectroscopy (XPS), EDS has a higher depth of analysis and can analyze the bulk material, rather than just characterizing the surface properties. This is useful in our case because we want to understand not only the surface modifications, but also if the magnetic fields affect the chemical composition within the substrate. The output of the EDS is a plot of intensity vs. kila-electron volts that shows the percentage of different chemical groups within a specific area.

3. RESULTS AND DISCUSSION

3.1 X-Ray Analysis

The experiments conducted at Argonne National Laboratory captured the processes with X-ray cameras. Various characteristics were recorded and analyzed for comparison, which will be observed and discussed in the following sections.

3.1.1 Keyhole Depth

The first analysis done using the x-ray images was for the keyhole depth. This was done by measuring the distance from the surface of the substrate to the bottom of the keyhole at each frame the laser was on, visualized in **Figure 3.1**. One of the purposes for measuring the keyhole depth is to visualize the average depth and variance of the keyhole. Measuring the average is useful for statistical calculations, however it does not entirely explain the change in depth. The other important statistic is variability, which describes how much the keyhole depth changes within the time-on. These values can be found from experimental measurements shown in **Table 3.1**.

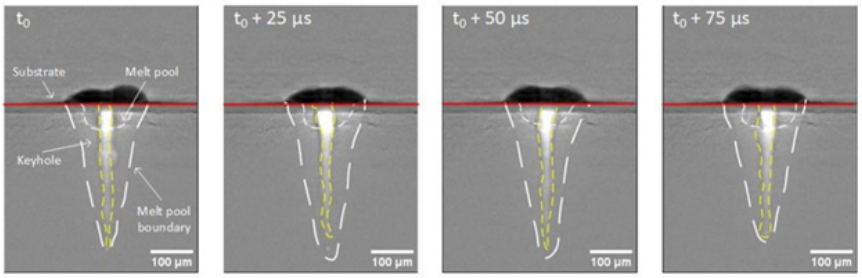

(a) Experiment 11

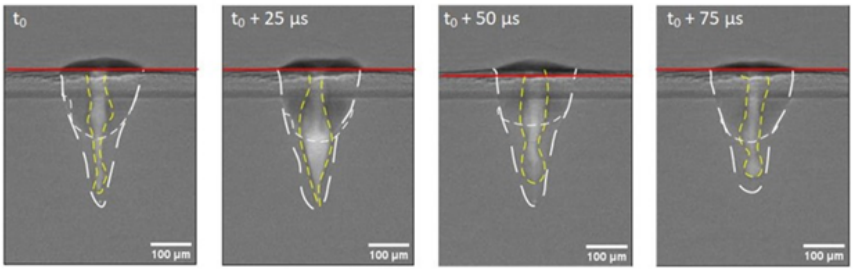

(b) Experiment 157

Figure 3.1: Time study of melt pool width of a) experiment 11 spot weld with parameters of 23% laser power and 1500 μs dwell time; b) experiment 157 spot weld with parameters of 23% laser power and 1500 μs dwell time

From this table, some results can be seen within groups of data. The first observation is that within the long magnet section, a higher laser power led to a greater increase in variance. Most of the experiments shown were done as spot welds, except for experiment 172, which was done as a line scan process. An interesting observation for the line scan experiment is that it has one of the highest averages in keyhole depths, however the variance is one of the lowest. This is important as it could explain the melt flow behavior, which is discussed later, but it could also be a reaction from either the movement of the laser or magnetic field.

Another measurement done within the realm of keyhole depths was to look at the variation in magnets to laser power. **Figure 3.2** can be used to visualize the variation in keyhole depth due to the variable of laser power, which is the only changing parameter between the experiments. It can be seen that experiment 1 had the highest keyhole depth due to the highest laser power, but

little variation in max/min data points. Experiments 11 and 48 are around the sample variation when looking at the different peaks of data points, while experiment 5 had the smallest change in keyhole depth. Looking at how the laser power variation alters the keyhole depth in the presence of magnets is useful as a baseline to understand what parameter is alterable to stay within a certain range of motion.

Table 3.1: Keyhole Depth Data

Experiment	**Magnet**	**Laser Power (%)**	**Average Depth (μm)**	**Variance (σ^2)**
1 (Spot)	Long Magnet	43	387.49	17617.75
5 (Spot)	Long Magnet	11.4	41.61	50.15
11 (Spot)	Long Magnet	23	271.71	4001.11
19 (Spot)	Long Magnet	23	282.37	4823.76
31 (Spot)	Long Magnet	23	287.60	3501.00
48 (Spot)	Long Magnet	23	302.06	3956.83
58 (Spot)	No Magnet	23	282.60	4800.05
59 (Spot)	No Magnet	23	251.76	4061.32
157 (Spot)	Ring Magnet	23	237.35	3467.69
159 (Spot)	Ring Magnet	23	245.33	3593.80
160 (Spot)	Ring Magnet	23	238.99	3723.20
173 (Line)	Long Magnet	43	374.95	1836.90

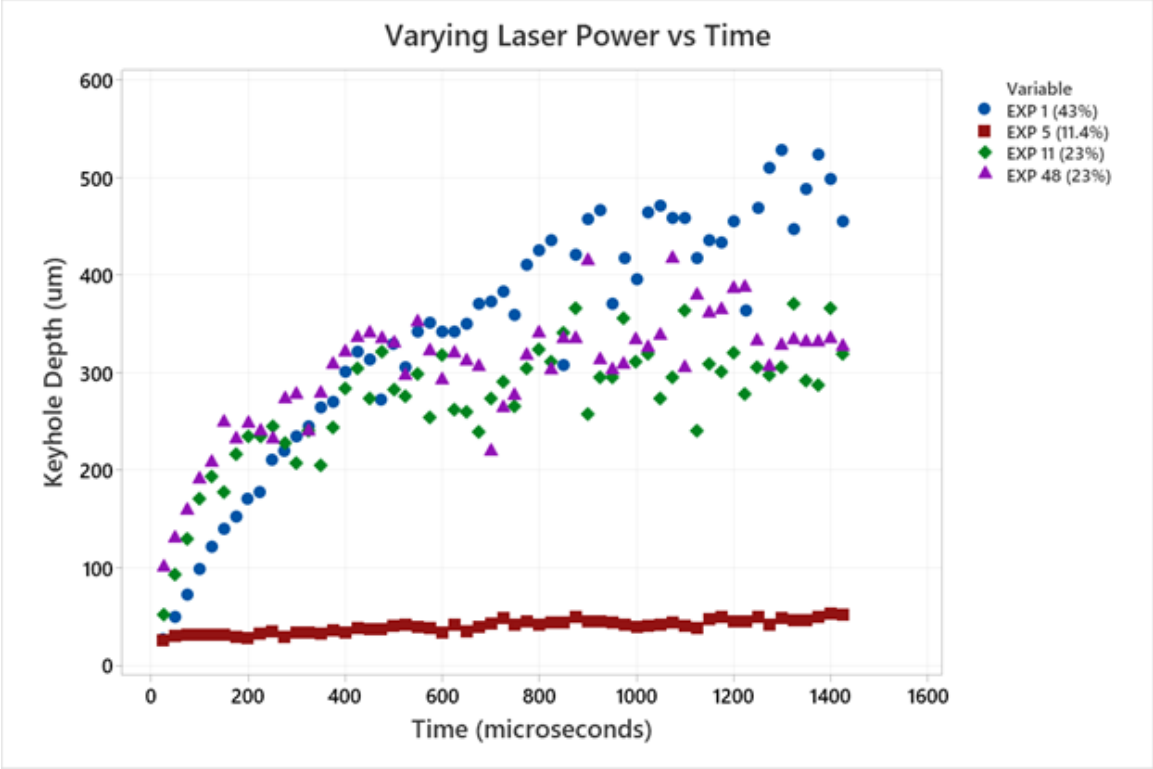

Figure 3.2: Measurements of keyhole depths through various experiments with similar process parameters with the main focus in laser power

Observing how the laser power effects the depth of the keyhole is important, but it does not capture the full picture of in-situ processing. **Figure 3.3** shows the comparison between experiments with the same laser power and dwell time, but a varying magnetic field distribution. This was done showing the change of magnets between a long, ring, and no magnetic field parameter. It can be seen that while the experiment with the ring magnet had the lowest keyhole depth average at 237.35 μm, it also had the lowest variance and variation in data points. Experiment 58, with no magnetic field, had the highest keyhole depth overall, but a greater distance between points recorded. A takeaway from this observation is that the magnetic fields alter the keyhole depth, considering the analyzed experiments were performed utilizing the same laser power. It is a promising factor for ring magnets in the area of reducing keyhole depth variation.

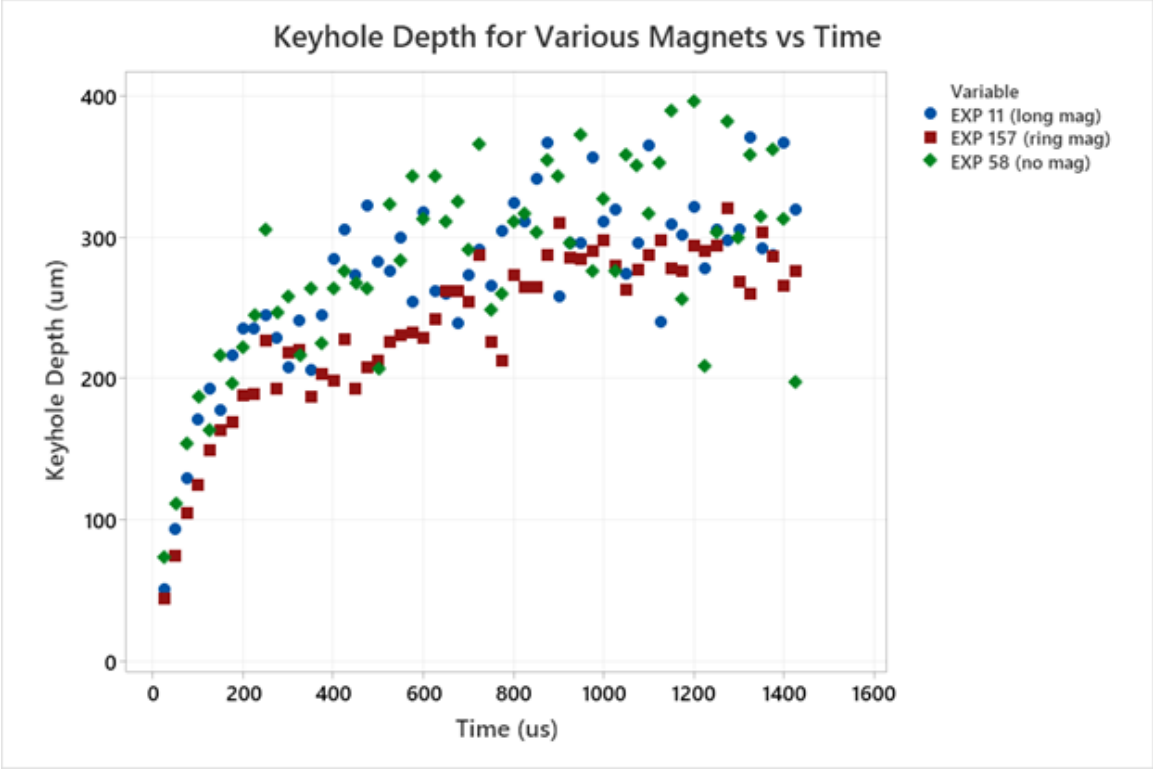

Figure 3.3: Measurements of three experiments: 11, 58, and 157. Each with similar processing parameters but various magnetic field distributions

Since it is difficult to visually observe a difference in data between the experiments, statistical analysis is needed to fully understand if adding magnets alters the keyhole. A one-way ANOVA (analysis of variance) test was performed on the same three experiments: 11, 58, and 157. ANOVA tests separate the data based on systematic factors and random factors. When there is no true variance between groups, then the F-Value is ideally around 1, which it is shown to be 7.77 in **Figure 3.4**. This means that there is some factor within the data that is making the results different. Another observation from the ANOVA tables is the 95% confidence performed within the Tukey Method. This method compares the means and variation to find correlation, then groups the experiments together that are similar. From the figure, it can be seen that experiment 58 and 11 share a common grouping variable, meaning they are not statistically significant from each other. However, experiment 157 is different from both experiment 58 and 11, showing statistically sig-

nificant difference in the data. This is one way to observe that ring magnets alter the experiment differently than long magnets.

Analysis of Variance

Source	DF	Adj SS	Adj MS	F-Value	P-Value
Factor	2	63593	31797	7.77	0.001
Error	168	687056	4090		
Total	170	750650			

Grouping Information Using the Tukey Method and 95% Confidence

Factor	N	Mean	Grouping
EXP 58	57	282.60	A
EXP 11	57	271.71	A
EXP 157	57	237.35	B

Means that do not share a letter are significantly different.

Figure 3.4: ANOVA and Tukey test for experiments 11, 58, and 157 to understand correlation and to test differences in means and variances. Statistics were recorded and analyzed in Minitab

On top of ANOVA tests, various Tukey tests were performed to test if there was statistically significant difference between the processes. Tukey tests are needed when three or more groups are mutually statistically significant. It can be shown in the boxplot represented in **Figure 3.5** that the experiments contain outliers near each other. These outliers represent the first few microseconds of on-time for the laser. However, comparing the boxes shows that experiment 157 is grouped in a somewhat lower region than 11 or 58. This boxplot can be used in tandem with the confidence interval in **Figure 3.5**, which visualizes the confidence interval simultaneous comparison for combinations of three experiments. It is clear to see that the confidence interval for 157 and 58 completely fall outside of the confidence interval for 58 and 11, meaning one of the experiments is statistically different than the others. Distinguishing which test causes the difference is more difficult to do with just confidence intervals.

The final statistical test to perform is to look at p-value comparisons between the data. This comparison is shown in **Figure 3.6**, which records the difference of means, 95% confidence interval, T-value, and adjusted p-value for each experiment combination. From the table in the figure, it is clear that experiment 157 is the clear deciding factor in statistical significance. This is shown from comparing the different p-values. The long magnet to ring magnet produced a p-value of 0.013 and the ring magnet to no magnet produced a p-value of 0.001. Since these p-values are less than an α of 0.05, the null hypothesis that these data points are from the same distribution can be rejected. This means that experiment 157 is statistically significant from the other two experiments, which proves that the ring magnet has a greater effect than no magnet or a long magnet on the keyhole depth.

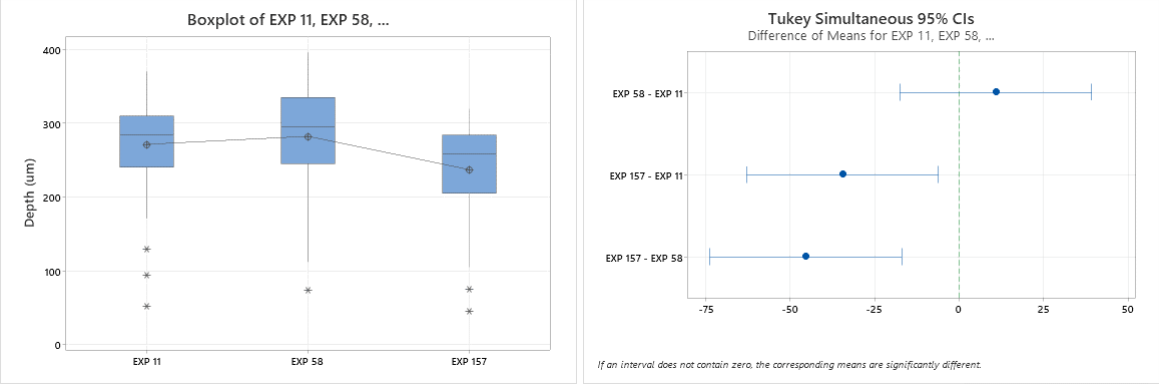

(a) Boxplot with outliers

(b) Tukey confidence interval

Figure 3.5: a) Box-plot of the three experiments differing in magnetic fields to observe where the different IQRs, means, and outliers lie within the data points measured; b) Tukey confidence interval for experiments 11, 58, and 157, with the comparison between each of them to visualize any similarities in the data

Tukey Simultaneous Tests for Differences of Means

Difference of Levels	Difference of Means	SE of Difference	95% CI	T-Value	Adjusted P-Value
EXP 58 - EXP 11	10.9	12.0	(-17.4, 39.2)	0.91	0.635
EXP 157 - EXP 11	-34.4	12.0	(-62.7, -6.1)	-2.87	0.013
EXP 157 - EXP 58	-45.3	12.0	(-73.5, -17.0)	-3.78	0.001

Individual confidence level = 98.07%

Figure 3.6: Tukey simultaneous test for difference in means for the three experiments that differ in magnetic field distributions

3.1.2 Melt Pool Width

Along with keyhole depth, another important melt pool characteristic to measure is the melt pool width. Melt pool width determines the surface area for printing, meaning it is vital in part tolerances. Measurements were made using ImageJ with the distance of the melt pool defined by the left tail of the melt pool to the right tail for each frame the laser was on. The melt pool width can be visualized by looking where the two white lines of the melt pool boundaries meet the substrate surface in **Figure 3.1**. This figure not only shows the melt pool on the surface, but also shows the melt pool within the substrate. This sub-melt pool is denoted by the smaller dotted-lined circles within the boundary layer, caused by the viewing angle of the x-ray camera. These melt pools are traveling in the z-direction, assuming the standard x and y planes. It is clear from the images that the melt pool is deeper with the ring magnet than the long magnet. Though no statistical comparison is made between the two sub-melt pools of experiments 11 and 157, it is an observation that could be analyzed in a future study. This study would look at the overall shape of the melt pool and how the magnetic field distribution can affect the depth and length from a different angle. The resulting melt pool width averages and variances can be seen in **Table 3.2**

Table 3.2: Melt Pool Width Data

Experiment	**Magnet**	**Laser Power (%)**	**Average Width (μm)**	**Variance (σ^2)**
1	Long Magnet	43	244.95	4210.42
5	Long Magnet	11.4	90.89	169.44
11	Long Magnet	23	150.14	2155.84
19	Long Magnet	23	171.62	1505.01
31	Long Magnet	23	174.98	2052.19
48	Long Magnet	23	161.71	952.23
58	No Magnet	23	172.48	2123.66
59	No Magnet	23	168.78	1770.88
157	Ring Magnet	23	165.66	1209.11
159	Ring Magnet	23	172.06	1337.46
160	Ring Magnet	23	154.9	1112.18

Figure 3.7 shows the experimentally measured melt pool widths for experiments 11, 58, and 157. These are the same from the keyhole measurements as they contain one of each magnets with the same parameters. As seen from the graph, each experiment generally follows a standard log-normal curve. However, from the graph it can be seen that the lack of a magnet caused the melt pool to reach an overall higher width for the time the laser was on.

Like the keyhole depth, a one way ANOVA and Tukey test were performed on the melt pool width for experiments 11, 58, and 157. The first test is the analysis of variance along with the Tukey grouping method, which can be seen in **Figure 3.8**. From the earlier analysis, the F-factor was explained that anything around 1 shows no true variance, however the melt pool width F-Value is 0.55. This value is the first example of visualizing the lack of variance between no magnet, long magnet, and a ring magnet in melt pool width. The three means also all share the same grouping, showing no difference from the data measured.

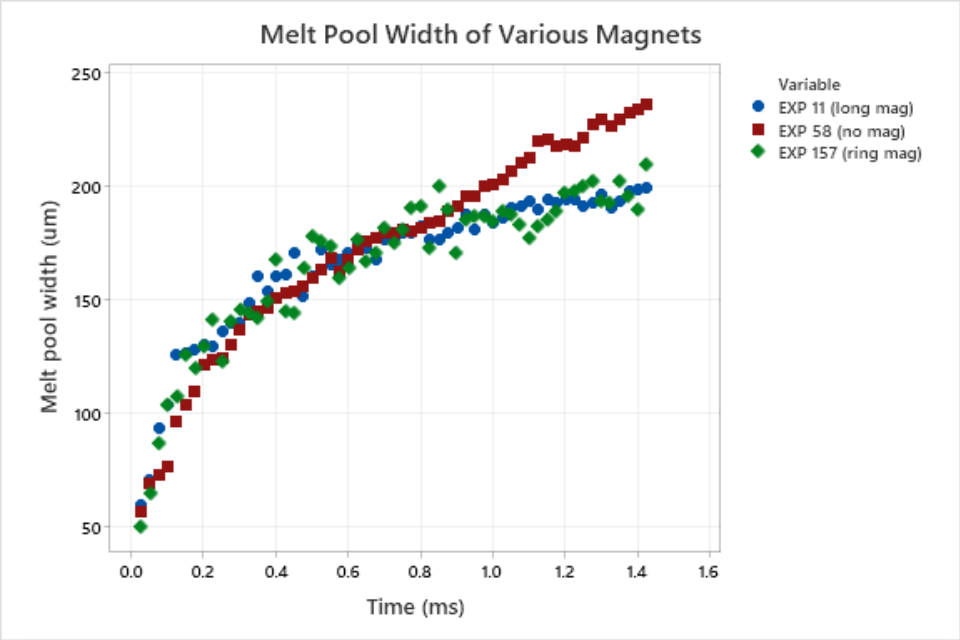

Figure 3.7: Measurements of the same three experiments as before, however the total melt pool distance is recorded and shown

Analysis of Variance

Source	DF	Adj SS	Adj MS	F-Value	P-Value
Factor	2	1599	799.4	0.55	0.576
Error	168	242706	1444.7		
Total	170	244305			

Grouping Information Using the Tukey Method and 95% Confidence

Factor	N	Mean	Grouping
EXP 58	57	172.48	A
EXP 11	57	166.40	A
EXP 157	57	165.66	A

Means that do not share a letter are significantly different.

Figure 3.8: ANOVA and TUKEY tests, showing the difference in the melt pool widths from the three experiments, recorded and created in MINITAB

A boxplot and Tukey simultaneous confidence interval can be seen in **Figure 3.9**. These graphs show the difference between each set of data compared to each other to find overlaps. From the graphs, all comparisons include zero in the interval, proving that the magnet does not make the experiments statistically significant. This comparison can also be seen in **Figure 3.10**, where the

p-values are shown for each experiment. Through the comparison of the p-values, it can be seen that none of them are less than the α value of 0.05, thus failing to reject that they are statistically different. In fact, the p-value for Exp 157 - Exp 11 is 0.994, meaning they are almost identical in terms of how the magnets affect the melt pool width.

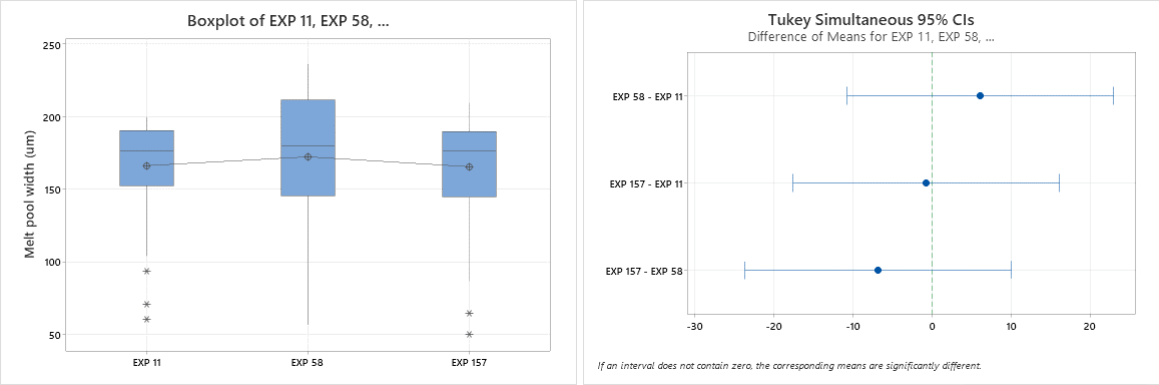

(a) Boxplot of melt pool widths

(b) Tukey confidence interval

Figure 3.9: a) Box-plot of the three experiments differing in magnetic fields to observe where the different IQRs, means, and outliers lie within the data points measured; b) Tukey confidence interval for experiments 11, 58, and 157, with the comparison between each of them to visualize any similarities in the data

Tukey Simultaneous Tests for Differences of Means

Difference of Levels	Difference of Means	SE of Difference	95% CI	T-Value	Adjusted P-Value
EXP 58 - EXP 11	6.09	7.12	(-10.73, 22.90)	0.86	0.669
EXP 157 - EXP 11	-0.73	7.12	(-17.55, 16.08)	-0.10	0.994
EXP 157 - EXP 58	-6.82	7.12	(-23.64, 9.99)	-0.96	0.604

Individual confidence level = 98.07%

Figure 3.10: Tukey test for difference of means, comparing the melt pool width data for the experiments. Recorded and analyzed in Minitab

Along with measurements, the melt pool of a width can be theoretically calculated using **Eq. 3.1**, found analytically in a study by El Cheikh *et al.* and observed by Sarah Wolff *et al.*

[43, 44]. The equation for theoretical melt pool width can be found below:

$$Width = \alpha \frac{P^{3/4}}{V^{3/4}} - 0.01 \qquad \text{(Eq. 3.1)}$$

where P is the laser power, V is the laser velocity, α is 1 in this case due to the lack of powder deposition [44]. The laser velocity can be found using **Eq. 3.2**, where t is the time in seconds and CR is the cooling rate of the melt pool in K/s. Cooling rate was found by running the generated Tiff images through MATLAB to plot the temperature of a specific spot in the experiment against time.

$$V = \frac{25.4t + \frac{2\alpha}{\log(CR)}}{t} \qquad \text{(Eq. 3.2)}$$

Towards the start of the graph, the values follow relatively similar distributions. Around the 0.25 ms mark however, the graphs split away from each other, showing that the measured values start to plateau. These equations do not account for a presence of a magnetic field induced, which would lead to the explanation of why the graph of the theoretical calculations and the actual experimental values is not similar. This can be seen in **Figure 3.11**.

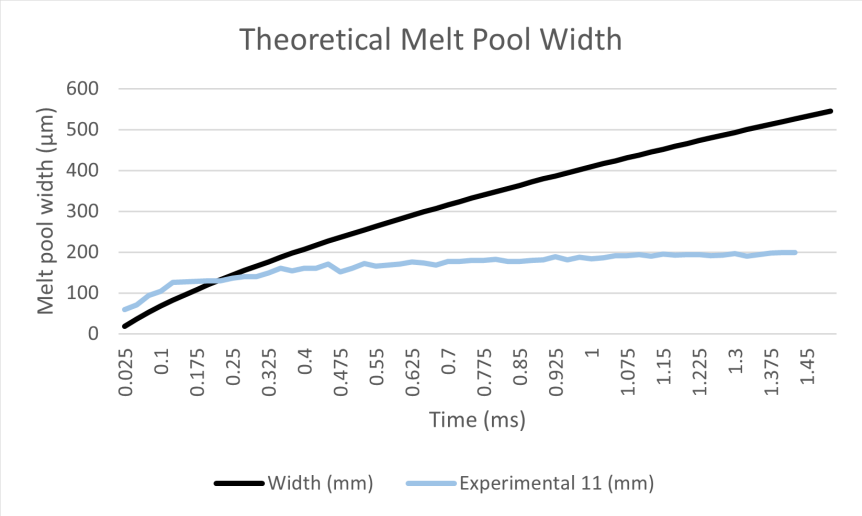

Figure 3.11: Theoretical melt pool width plotted with the experimental measurements of experiments 11, with long magnet.

3.1.3 Melt-Flow Dynamics

In order to understand how magnetic fields affect the particle velocity and melt flow behavior, a 'settling' velocity is needed. This velocity can be solved using **Eq. 3.3**, which follows Stoke's Law. This equation is theoretically how fast the particle should be moving within the specific fluid, given a measured diameter for the particle:

$$\nu_p = \frac{\rho_p - \rho_f}{\gamma \mu_f} g d_p^2 \qquad \text{(Eq. 3.3)}$$

where g is the gravitational acceleration, ρ_p is the mass density of the tungsten particle, d_p is the diameter of the tungsten particle, ρ_f is the mass density of the fluid, γ is the coefficient which depends on the fluid and particle velocity, and μ_f is the dynamic viscosity of the fluid [45, 46].

We can use this settling velocity to compare to the experimentally measured velocities of the particles. Three tungsten particles were tracked near the keyhole of the line-scanning experiment. Particle 1 is a tracked particle near the surface of the substrate, particle 2 is near the center of the keyhole, and particle 3 is at the bottom of the keyhole. Within ImageJ, a third party program by the name of TrackMate was used to measure the velocities [47]. This was done to observe how the flow changes depending on the location of the particle with respect to the keyhole. The settling velocity, ν_p, was calculated to be 6.49×10^{-4} m/s, 4.45×10^{-4} m/s, and 5.2×10^{-4} m/s, for particles 1, 2, and 3, respectively. The measured particles were tracked to be 6.43×10^{-2} m/s, 3.52×10^{-2} m/s, and 3.19×10^{-2} m/s. One of the reasons the measured velocities are an order of magnitude higher is due to the undulation and positioning of the laser. The other reason these velocities are so much faster could be by the affect from the magnetic fields, represented in **Figure 3.12**.

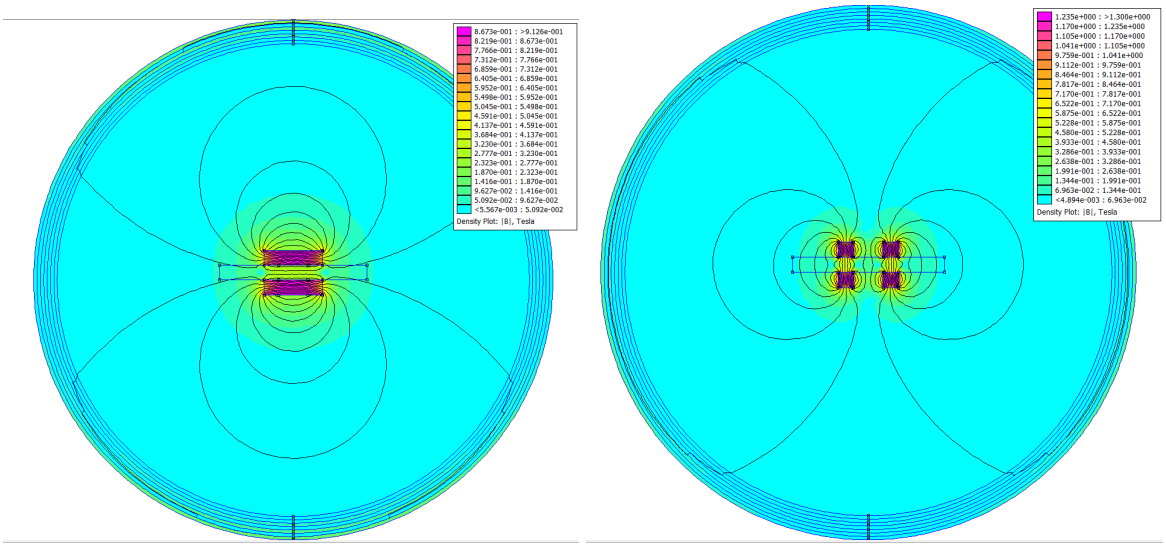

(a) (b)

Figure 3.12: a) Magnetic fields of the Long Magnet; b) and the Ring Magnet as they would affect the sample.

Figure 3.13 can be used to visualize the velocities of the three tracked particles. From this observation, it can be seen that particles 1 and 3 had the most variation in the data. This can be seen by the random jumps from sharp peaks to valleys. This can be compared with the graph of particle 2, which shows a relatively more steady state to the motion of the particle. One possibility of this is the location of the particle. This shows the idea of chaotic change and different viscosity gradients within the melt pool. Particle 1 is near the surface, subject to the laser movement and interactions with other particles near the surface. Particle 3 is at the tail of the keyhole, which would be subject to a possible lower viscosity, but also the influence of constant fluctuations in tail length. In contrast, particle 2 is near the center, where the keyhole is not whipping around and there are less interactions with the environment. The velocities can be found in **Table 3.3** and **Table 3.4**, while the direction of flows can be seen in **Figure 3.14**.

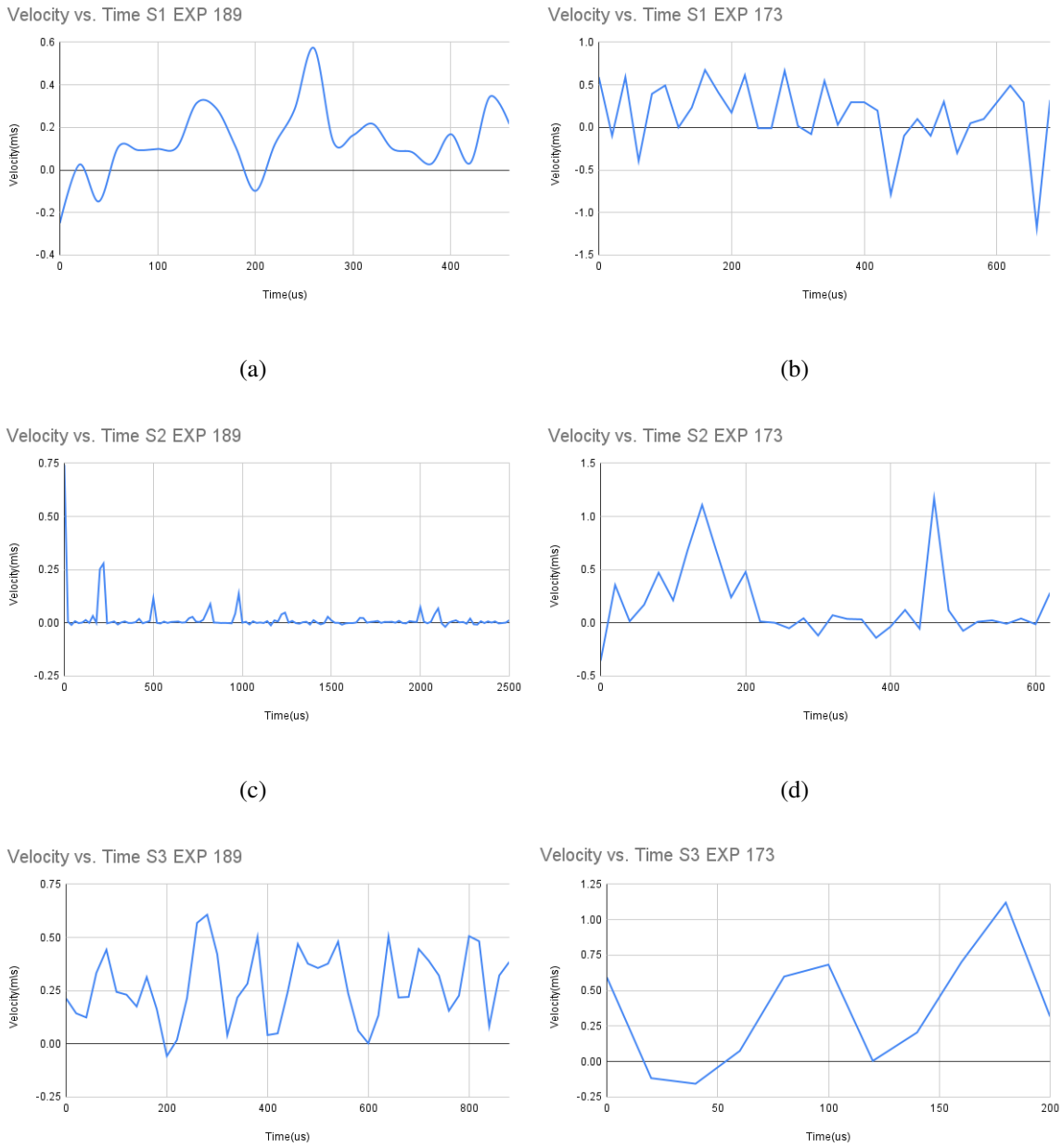

Figure 3.13: Tracking of experiment 173 with a long magnet and experiment 189 without any magnets. Both experiments had a scan speed of 300 mm/s, and laser power of 35% a, b) measurement of the tungsten particle near the top of the keyhole, near and interacting with the surface of the substrate; c, d) tungsten particle velocity in the middle of the keyhole where the turbulent flow is less than the surface; e, f) tungsten velocity near the bottom of the keyhole where the flow is in a chaotic state.

Table 3.3: Experiment 189 No Magnet

Location	**Avg Speed** (m/s)	**Variance** (σ^2)
S1	0.130	0.028
S2	0.022	0.008
S3	0.273	0.028

Table 3.4: Experiment 173 Long Magnet

Location	**Avg Speed** (m/s)	**Variance** (σ^2)
S1	0.150	0.156
S2	0.173	0.164
S3	0.366	0.115

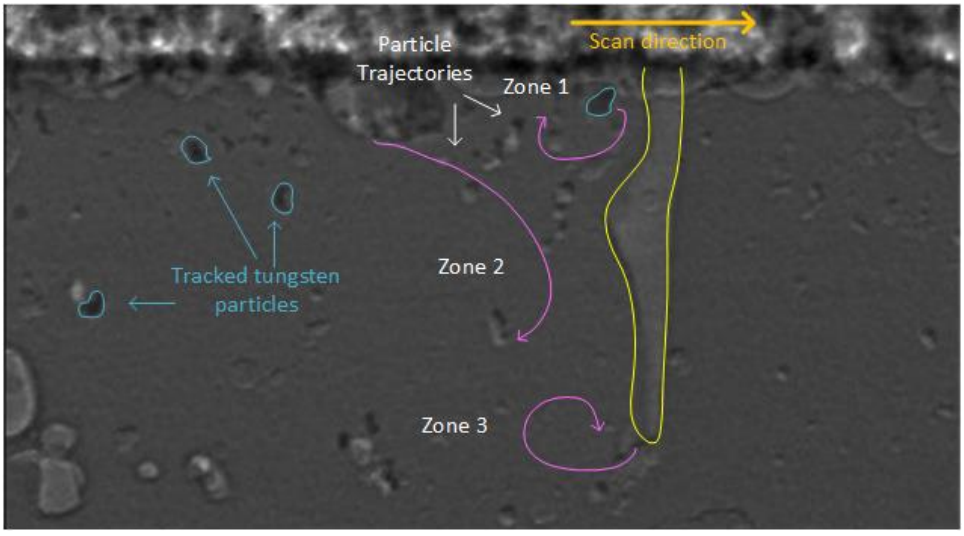

Figure 3.14: X-ray annotation of experiment 173 that visualizes the flow of the tungsten particle path and trajectory.

Marangoni flow is a common phenomenon that occurs in the liquid melt pool. This force is the result of temperature gradients, which occur from the change in surface tension of the substrate. The surface tension with respect to temperature for the material is needed, which can be found using **Eq. 3.4**.

$$\frac{\partial \sigma}{\partial T} = -A - \Gamma_s \cdot R \cdot \ln(1 + \alpha_s \cdot k_1 \cdot \exp\left(-\frac{\Delta H_0}{RT}\right)) - \frac{\alpha_s \cdot \Gamma_s \cdot \Delta H_0 \cdot k_1 \cdot \exp\left(-\frac{\Delta H_0}{RT}\right)}{T(1 + \alpha_s \cdot k_1 \cdot \exp\left(-\frac{\Delta H_0}{RT}\right)} \quad \text{(Eq. 3.4)}$$

where σ is the surface tension of pure metal; Γ_s is surface excess at saturation; A is the absolute value of the coefficient for temperature; α_s is the active element activity; R is the universal gas constant [45]. Due to lack of certain captured data, the surface tension was estimated using known values and experimentally captured results from previos studies. This estimation makes the surface tension around -4.81×10^{-4} at a temperature of $1700°C$, measured by Livio Battezatti *et al.* [48]. This result was chosen as the temperature of the experiment was around $1700°C - 1800°C$, measured from the IR camera during experimentation.

This surface tension can be used to then find the Marangoni flow number (Ma), which is a unit-less number used to evaluate the relative effect of the Marangoni flow over liquid viscosity as [45]:

$$Ma = -\frac{\partial \sigma}{\partial T} \cdot \frac{L \Delta T}{\mu \alpha} \quad \text{(Eq. 3.5)}$$

where $\frac{\partial \sigma}{\partial T}$ is the surface tension, L is the length of the melt pool, ΔT is the temperature, μ is the dynamic viscosity of Ti64, and α is the thermal diffusivity of Ti64 [46, 49]. We found the Marangoni flow number to be approximately 216.0175 which indicates a relatively low Marangoni flow between the Ti64 and the Tungsten trackers in the melt pool. Introducing the magnetic field could be the reason why this value is relatively low, however due to the lack of data, further calculations are not viable.

3.2 Results of SEM and EDS

Scanning electron microscopy (SEM) is an important observation method that is used to visualize the microstructure and surface topology, both of which are surface characterization techniques. In tandem with SEM, energy dispersive x-ray spectroscopy (EDS) can be done to quantitatively count the chemical composition of the sample. With EDS, there are two types of images that can be captured. The first image captured is the live sum spectrum of compounds found within marked areas on the sample, which can be seen in **Figure 3.15**. This electron scattered image can be used to understand formations and compositions on different parts of the sample. It can be used in tandem with the EDS spectrum, shown in **Figure 3.15**. The sample image produced shows the concentration field of materials within the area of observation, which can be seen in **Appendix A**.

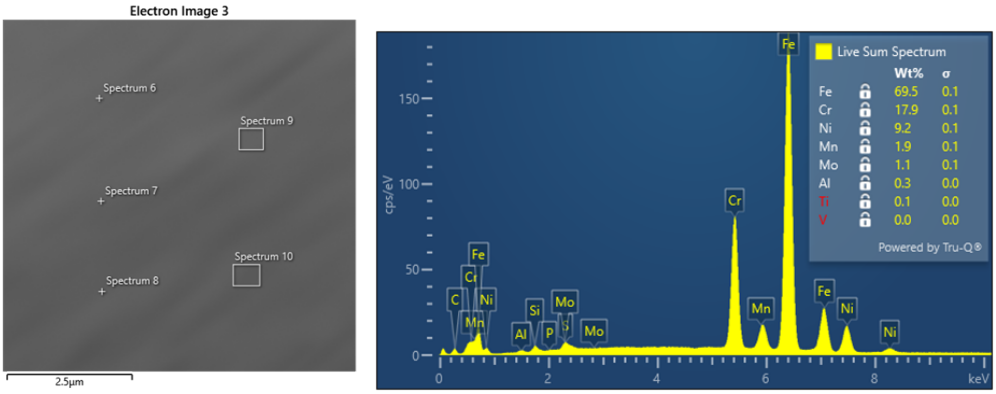

(a) Electron Image (b) Spectrum Recording

Figure 3.15: a) SEM image of sample 9 with long magnet, scan speed of 300 mm/s, and a laser power of 55% with SS316L and Ti64; b) chemical composition captured and visually located on the image, denoted by the respective spectrum.

The spectrum of the sample printed within the magnetic field shows a relatively high composition of iron (Fe) and chromium (Cr) at 69.5% and 17.9%, respectively. On the other hand, the composition of Ti, Al, and V are extremely low. This does not necessarily mean these are the chemical compositions of the whole part, but it does focus the attention to the adhesion and mixing

of the materials. In this case, we want to focus on the SS316L binding with Ti64 since SS316L is able to create a good passivaing layer from the chromium and oxygen formation.

3.3 Results of Ti64 and Stainless Steel 316L Composite

The printing of SS316L on Ti64 using the custom built DED machine can be seen in **Figure 3.16**. The purpose of observing these experiments is to understand the affect of focal distance and dwell time on the spot welding experiments. An interesting observation is in the bottom left spot on the focal distance tests. It can be seen that a solid steel ball was formed, most likely caused by a slight fluctuation in the powder layer in combination with a 30% laser power and 210 mm focal distance from part to laser. The experiments were conducted with a powder height of 0.3-0.6 mm of material on top of the substrate. Standard practice involves a layer height of around 0.1 mm, but we wanted to test the viability of increasing the height in certain areas for greater adhesion or part formation.

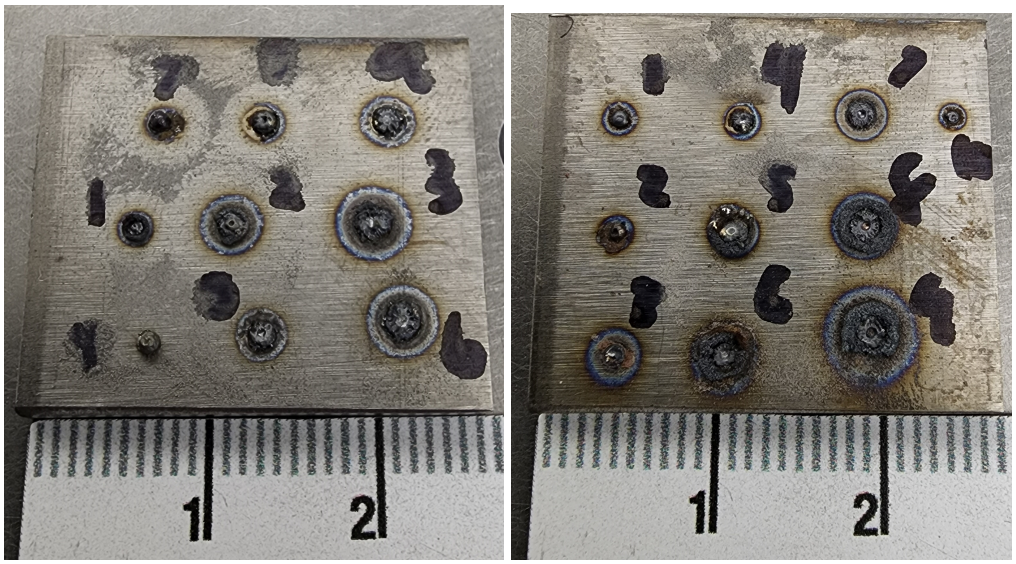

(a) Focal Distance (b) Dwell Time

Figure 3.16: a) SS316L printed on Ti64 substrate where left to right is 30%, 50%, and 70%, and top to bottom rows are at a focal distance of 192, 200, and 210 mm, respectively; b) 1-3 at laser power of 30%, 4-6 at 50%, and 7-9 at 70%, with each row being at 3-5-7 second dwell time.

3.4 Results of Ti64 and Hydroxyapatite Composite

Printing the HAp and Ti64 composite proved to be more difficult for a few reasons. The first reason is that the HAp supplied by the manufacturer contains a certain chemical formula, denoted in **Table 2.1**. This specific composition causes the HAp to have a melting temperature of $1700°C$, which is close to the melting temp of Ti64, around $1600°C$. Melting temperature is not completely the issue here however as the laser has no issue reaching that degree of temp. During experimentation, it was observed that the powder would start to heat and cause an expansion, as if it was forming an air pocket or melting 'bubble.' After a few seconds, the HAp would create a hole and expose the substrate. A time study was done to see how long it took for the laser at 80% power to punch through the powder. The recorded times were 1.8, 2, 3, and 5.8 seconds, with an average of 3.15 seconds. This time was noticed to be semi-dependent on the thickness of the layer of HAp, which was around 0.3 to 0.5 mm. Results of these specific dwell times can be seen in **Figure 3.17**. It should be noted that these results are preliminary, with the purpose being validity for forming a HAp-Ti64 composite through laser manufacturing. Next steps would be to look at the microstucture and EDS of the newly formed parts to understand the material bonding through this process.

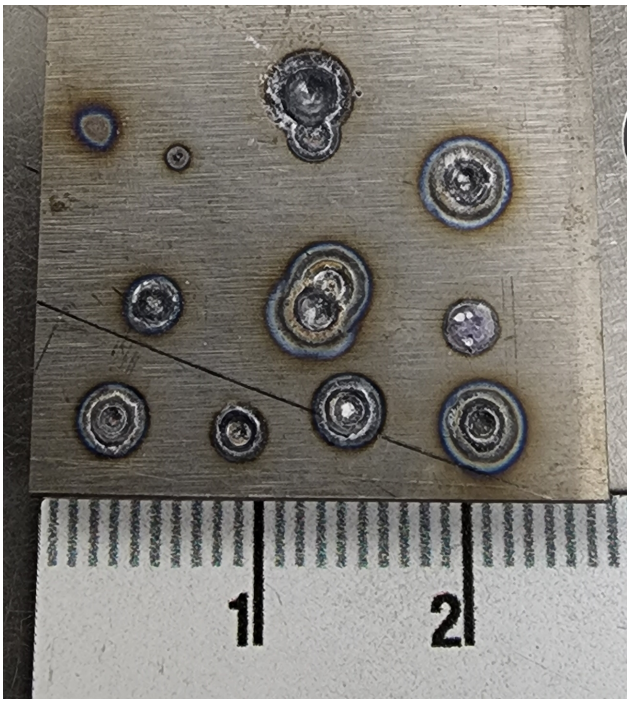

(a) Full scale image

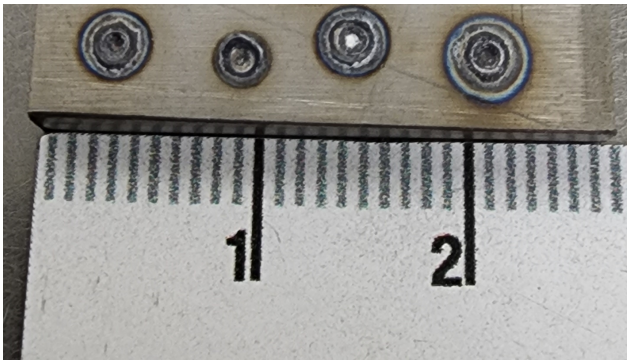

(b) 80% Laser power concentration

Figure 3.17: a) LPBF printing of hydroxyapatite on a Ti64 substrate; b) bottom layer of spots can be seen that were printed with a laser power of 80%, while the others differed between 70% and 100% to find the optimal percentage for melting.

4. CONCLUSION

4.1 Spot Welding

4.1.1 Changes due to Laser Power

When we focus exclusively on keyhole depth in these experiments we begin to see how a variety of factors affect not only its depth but its variance. As shown in **Figure 3.2** laser power directly correlates with keyhole depth and variance of measurements which is to be expected. With more energy being added to the material the easier it is to create a larger keyhole regardless of magnetic fields however, it is also more difficult to control where the energy goes. This explains the increase in variance seen in our results, which stands true for both melt pool and keyhole depth.

4.1.2 Changes due to Magnets

The effects caused by the magnets are not as intuitive as those brought on by increasing or decreasing laser power, due to the difference in magnetic field strength and orientation relative to the position of the magnet it is difficult to say what exactly is causing the differences we see in our results. In **Table 3.1** we can clearly see that adding a magnet to the testing environment significantly reduces the variance of the keyhole depth while in the case of the long magnet increasing the average keyhole depth and decreasing it in the case of the ring magnet. This difference is most likely due to the different orientation of the magnetic fields shown in **Figure 3.12**. We can see that the magnetic field of the ring magnet is mostly pointed perpendicular to the direction of the laser and therefore the flow of the liquid, hindering its movement in the X or Y directions while potentially increasing the displacement in the Z direction. While the long magnets produce a magnetic field parallel to that of the flow which would increase the movement in the X or Y directions.

The melt pool showed less significant changes when compared to the keyhole depth shown in **Figure 3.7** we can clearly see that as time progresses the experiment without a magnet had larger melt pool width when compared to both experiments that had magnets. When we compare the ring and long magnets we see an opposite effect as the keyhole depth, the ring magnet seems to

increase variation while the long magnet looks to be significantly more consistent throughout time. If our previous assumptions of the magnetic fields is correct then it would make sense that they would have opposite effects when you change the axis, if it increases the flow in the X direction it will most likely decrease the flow in either the Y or Z direction.

4.2 Melt-Flow Dynamics

Melt-Flow Dynamics can be more complicated to analyze when compared to spot welding due to the increased amount of variables and areas of focus. If we look at **Figure 3.14** we can see that the particles are categorized in three main zones, depending on the zone the particle can be undergoing different forces, viscosities, and temperatures which can change the material properties quite drastically.

4.2.1 Changes due to Magnets

In order to start our analysis of magnetohydrodynamics we have to look at the difference in the control velocity from the theoretical settling velocity the fluid should have. We can see that all of the theoretical values were roughly two orders of magnitude smaller than our calculated values for the particles. This is probably due the movement and energy deposition of the laser, these theoretical values assume that the fluid is undisturbed and they do not account for the addition of energy.

If we look at **Figure 3.13** we can begin to see the general effect that the magnet has on the flow of molten metal. When we compare **Table 3.3** and **Table 3.4**, which are the average speed and variance for experiment 173 and 189 respectively, we can see quite clearly that the average speed in each flow regime has increased by at least 15% and the variance has increase far more substantially by at least 311%. The increase in velocity is most likely due to the orientation of the magnetic field being mostly aligned with the direction of the flow being measured. However, the most probable reason for the drastic increase in variance is due to our measurements only considering the X direction. Since magnets affect a three dimensional area around them it is likely that they caused some movement in the Y and Z directions as mentioned in the Effects of Magnets

on Spot Welding section.

Further research can be improved with the addition of another X-Ray camera viewing the Y-Z plane to better understand the motion of the tungsten particles and therefore a more detailed understanding of how the magnets can affect the molten metal and the flow of particles within it.

4.2.2 Changes due to Internal Fluid Forces

The primary force affecting the fluid is the hydraulic pressure caused by the movement of the fluid and its incompressible nature. This force might not have a significant affect when comparing EXP 189 and EXP 173 due to the only change in variable between them being the long magnet, therefor they would both experience a similar hydraulic pressure.

Marangoni flow happens in fluids with areas of different temperatures, however due to our relatively low Marangoni flow number of approximately 216 we can assume that it had a negligible affect on the fluid dynamics of this experiment. It is possible that the magnetism affected the low Marangoni flow number but further studies are required for a definitive answer.

4.3 SEM and EDS

From the results discussion, we were able to observe a high concentration of Fe and Cr and a low concentration of Ti, Al, and V within the SS316L and Ti64 composite printed within a magnetic field. This leads us to believe that the two materials are not mixed, since Fe and Cr come from SS316L, and The other three come from Ti64. Ideally, the SS316L powder would be distributed evenly along the surface of the Ti64 substrate, and the concentration difference between the materials would not be as large.

4.4 DED Composites

It is evident from an observation of **Figure 3.16** that the overall printing process requires more refinement. Compared to the LPBF printing conducted in the magnetic augmentation section, the properties of the DED printer being used is relatively unexplored. This leads to a greater emphasis being placed on qualitative results while the intricacies of printing using this machine evolve further.

4.4.1 Ti64 and SS316L Composite

From the prints using this composite it is evident that an increase in laser power or dwell time both result in and undesirable ring of poorly bonded print material around the spot welding area. The goal of these spot welding tests is to find some approximate process parameters to easy the transition to more complex printing types, such as line scanning. The best melt pattern occurs when a balance is struck between dwell time. Looking at **Figure 3.16** b) a viable spot weld was generated when the laser was set to seventy percent power with a dwell time of three seconds. This representative of the maximum laser power tested with the minimum dwell time. The inverse arrangement also resulted in a good print with laser power set to thirty percent and a dwell time of seven seconds. This suggests that dwell time and laser power have an interchangeable relationship and that for the purpose of larger scale prints a higher laser power, as opposed to a longer dwell time, will result in more efficient print times, while still maintaining the quality of the print.

4.4.2 Ti64 and HAp Composite

From **Figure 3.17**, it was shown that the binding capabilities of the HAp on Ti64 was not optimal. We observed the printing to more difficult with the powder and adhesion of HAp. The issue lies within the differing thermal diffisivity and absorption between the two components of the composite. Effectively, the laser just displaced the HAp and melted through the substrate before the HAp melted to a significant degree. Possible solutions include a more thorough exploration of different focal distances and laser powers in order to optimize the process. Additionally, while it is not specifically relevant to this composite, a substrate with a lower rate of thermal absorption could be used.

4.5 Further Work

Future research can be done to optimize the processes observed in this paper and to expand upon the work done. A more in depth-analysis can be performed to quantify the magnetic effect on the flow and thermal properties of the materials within the additive manufacturing process. This could include modeling and simulations of the process for theoretical studies and then experimen-

tally comparing the two. An important note would be how to alter the equations to account for all variability within the magnetic field inside the substrate during the printing process.

Other work can involve measuring certain surface characteristics, analyzing the melt flow from different perspectives, testing the mechanical strength of the magnetically affected parts, and refining the printing viability for Ti64/SS316L with HAp for bio-implementation.

REFERENCES

[1] M. Niinomi, "Mechanical properties of biomedical titanium alloys," *Materials Science and Engineering: A*, vol. 243, pp. 231–236, 1998.

[2] J. Slotwinksi, "Porosity measurements and analysis for metal additive manufacturing process control," *Journal of Research of the National Institute of Standards and Technology*, vol. 119, pp. 494–528, 2014.

[3] B. Zhang, "In-process monitoring of porosity during laser additive manufacturing process," *Additive Manufacturing*, vol. 28, pp. 497–505, 2019.

[4] J. Ning, "Analytical modeling of part porosity in metal additive manufacturing," *International Journal of Mechanical Sciences*, vol. 172, 2020.

[5] Z. Sun, "Reducing hot tearing by grain boundary segregation engineering in additive manufacturing: example of an alxcocrfeni high-entropy alloy," *Acta Materialia*, vol. 204, 2021.

[6] S. Thapliyal, "Segregation engineering of grain boundaries of a metastable fe-mn-co-cr-si high entropy alloy with laser-powder bed fusion additive manufacturing," *Acta Materialia*, vol. 219, 2021.

[7] W. Zhou, "Inhibition of cracking by grain boundary modification in a non-weldable nickel-based superalloy processed by laser powder bed fusion," *Materials Science and Engineering: A*, vol. 79, 2020.

[8] S. Lee, "Data analytics approach for melt-pool geometries in metal additive manufacturing," *Science and Technology of Advanced Materials*, vol. 20, 2019.

[9] A. Nassar, "Formation processes for large ejecta and interactions with melt pool formation in powder bed fusion additive manufacturing," *Scientific Reports*, vol. 9, 2019.

[10] P. Cook, "Simulation of melt pool behaviour during additive manufacturing: Underlying physics and progress," *Additive Manufacturing*, vol. 31, 2020.

[11] J. D. Avila, "Additively manufactured ti6al4v-si-hydroxyapatite composites for articulating surfaces of load-bearing implants," *Additive Manufacturing*, vol. 34, 2020.

[12] S. Wolff, "Anisotropic properties of directed energy deposition (ded)-processed ti–6al–4v," *Journal of Manufacturing Processes*, vol. 24, pp. 397–405, 2016.

[13] J. Alcisto, "Tensile properties and microstructures of laser-formed ti-6al-4v," *Journal of Materials Engineering and Performance*, vol. 20, pp. 203–212, 2011.

[14] R. G. Bernd Baufeld, Omer Beist, "Additive manufacturing of ti–6al–4v components by shaped metal deposition: Microstructure and mechanical properties," *Materials & Design*, vol. 31, pp. 106–111, 2010.

[15] J. D. Avila, "Hydroxyapatite reinforced ti6al4v composites for load-bearing implants," *Acta Biomaterialia*, vol. 123, pp. 379–392, 2021.

[16] K. Zhang, "Characterization of stainless steel parts by laser metal deposition shaping," *Materials and Design*, vol. 55, pp. 104–119, 2014.

[17] A. M. Beese, "Effect of processing parameters on microstructure and tensile properties of austenitic stainless steel 304l made by directed energy deposition additive manufacturing," *Acta Materialia*, vol. 110, pp. 226–235, 2016.

[18] H. Zhang, "Electromagnetically confined weld-based additive manufacturing," *Procedia CIRP*, vol. 6, pp. 515–520, 2013.

[19] L. Wang, "Thermoelectric magnetohydrodynamic model for laser-based metal additive manufacturing," *Physical Review Applied*, vol. 15, 2021.

[20] M. Zeng, "Evolution phenomena and surface shrink of the melt pool in an additive manufacturing process under magnetic field," *International Journal of Heat and Mass Transfer*, vol. 123, pp. 760–775, 2018.

[21] I. Nlebedim, "Functionalizing magnet additive manufacturing with in-situ magnetic field source," *Additive Manufacturing*, vol. 34, 2020.

[22] W. Y, "Texture control of inconel 718 superalloy in laser additive manufacturing by an external magnetic field," *Materials Science*, 2019.

[23] S. P, "Magnetic manipulation in directed energy deposition using a programmable solenoid," *Materials Processing Technology*, vol. 299, 2022.

[24] S. L. Sing, "Laser powder bed fusion for metal additive manufacturing: perspectives on recent developments," *Virtual and Physical Prototyping*, vol. 15, pp. 359–370, 2020.

[25] A. Sidambe, "Metal injection moulding of cp-ti components for biomedical applications," *Journal of Materials Processing Technology*, vol. 212, pp. 1591–1597, 2012.

[26] R. K. Quinn, "Electrochemical and surface analytical characterization of titanium and titanium hydride thin film electrode oxidation," *Journal of The Electrochamical Society*, vol. 125, pp. 1790–1798, 1978.

[27] G. Shibo, "Powder injection molding of ti-6al-4v alloy," *Journal of Materials Processing Technology*, vol. 173, pp. 310–314, 2006.

[28] C. Elias, "Biomedical applicaitons of titanium and its alloys," *Biological Materials Science*, pp. 46–49, 2008.

[29] A. T. Sidambe, "Biocompatibility of advanced manufactured titanium implants-a review," *Materials*, vol. 7, pp. 8168–8188, 2014.

[30] E. Bidaux, "Metal injection moulding of low modulus ti–nb alloys for biomedical applications," *Powder Metallurgy*, pp. 263–266, 2013.

[31] P. S, "In vivo performance of selective electron beam-melted ti-6al-4v structures," *Journal of Biomedical Materials Research*, pp. 56–62, 2009.

[32] R. Mller, "Surface engineering of stainless steel materials by covalent collagen immobilization to improve implant biocompatibility," *Biomaterials*, vol. 26, pp. 6962–6972, 2005.

[33] J. Walczak, "In vivo corrosion of 316l stainless-steel hip implants: morphology and elemental compositions of corrosion products," *Biomaterials*, vol. 19, pp. 229–237, 1998.

[34] M. Fathi, "In vitro corrosion behavior of bioceramic, metallic, and bioceramic–metallic coated stainless steel dental implants," *Dental Materials*, vol. 19, pp. 188–198, 2003.

[35] M. Dewidar, "Processing and mechanical properties of porous 3 16l stainless steel for biomedical applications," *Transaction of Nonferrous Metals*, pp. 468–473, 2007.

[36] H. F. Morris, "Hydroxyapatite-coated implants: A case for their use," *Oral and Maxillofacial Surgery*, vol. 56, pp. 1303–1311, 1998.

[37] J. N. Kent, "Evaluation of hydroxylapatite-coated titanium dental implants in dogs," *Oral and Maxillofacial Surgery*, vol. 45, pp. 601–607, 1987.

[38] M. S. Block, "Advantages and disadvantages of hydroxylapatite-coated implants," *Oral and Maxillofacial Surgery*, vol. 3, pp. 835–851, 1991.

[39] K. Eliceiri, "Nih image to imagej: 25 years of image analysis," *Nature Methods*, vol. 9, pp. 671–675, 2012.

[40] K. Eliceiri, "Fiji: an open-source platform for biological-image analysis," *Nature Methods*, vol. 9, pp. 676–682, 2012.

[41] I. Yadroitsev, "Selective laser melting of ti6al4v alloy for biomedical applications: Temperature monitoring and microstructural evolution," *Journal of Alloys and Compounds*, pp. 404–409, 2014.

[42] Y. Leng, *Materials Characterization Introduction to Microscopic and Spectroscopic Methods*. Wiley-VCH, 2013.

[43] E. Cheikh, "Prediction and analytical description of the single laser track geometry in direct laser fabrication from process parameters and energy balance reasoning," *Journal of Materials Processing Technology*, vol. 212, 2012.

[44] S. Wolff, "Synchronized in situ x-ray and infrared imaging of laser deposition," *Manufacturing Letters*, vol. 31, 2022.

[45] Q. Guo, "In-situ full-field mapping of melt flow dynamics in laser metal additive manufacturing," *Additive Manufacturing*, vol. 31, 2020.

[46] R. Wunderlich, "Surface tension and viscosity of industrial ti-alloys measured by the oscillating drop method on board parabolic flights," *High Temperature Materials and Processes*, pp. 671–675, 2011.

[47] D. Ershov, "Bringing trackmate into the era of machine-learning and deep-learning," *BioRxiv*, 2021.

[48] L. Battezatti, "Surface tension and viscosity of industrial alloys from parabolic flight experiments - results of the thermolab project," *Microgravity - Science and Technology*, vol. 16, 2005.

[49] E. Fereiduni, "Selective laser melting of hybrid ex-situ/in-situ reinforced titanium matrix composites: Laser/powder interaction, reinforcement formation mechanism, and non-equilibrium microstructural evolutions," *Materials Design*, vol. 184, 2019.

APPENDIX A: EDS CHEMICAL COMPOSITIONS

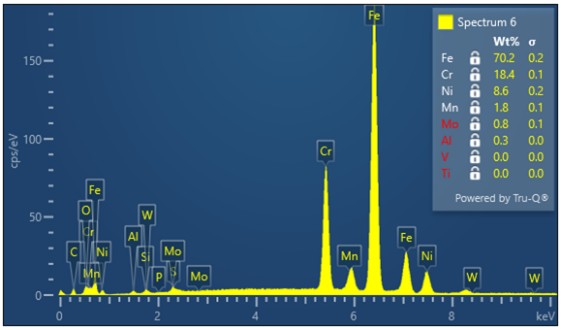

(a)

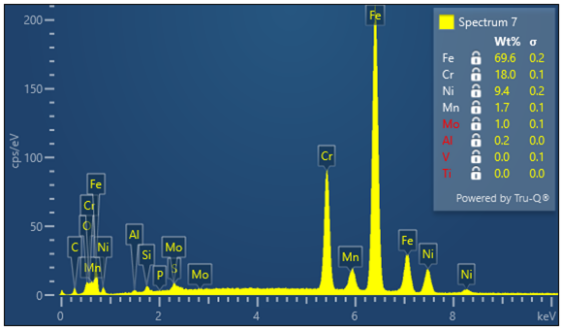

(b)

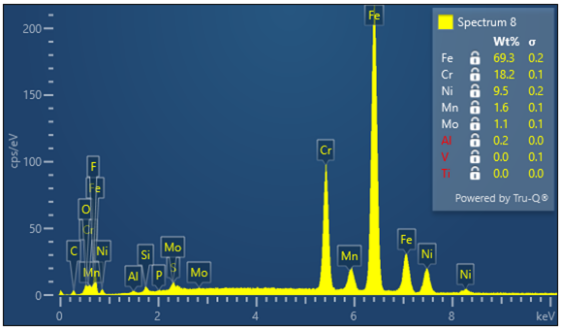

(c)

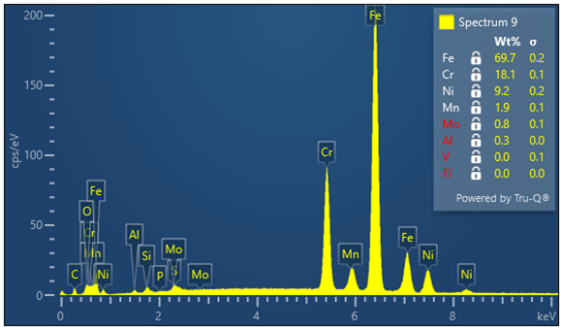

(d)

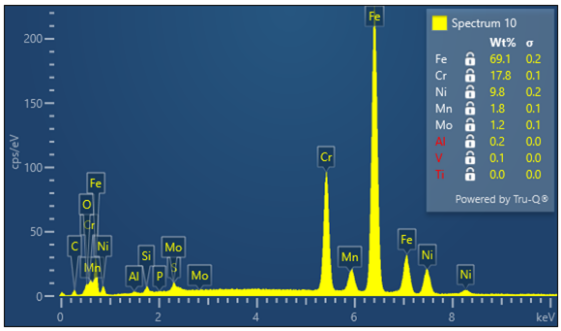

(e)

Figure A.1 Spectrum mapping of the different areas on the material showing their respective chemical composition

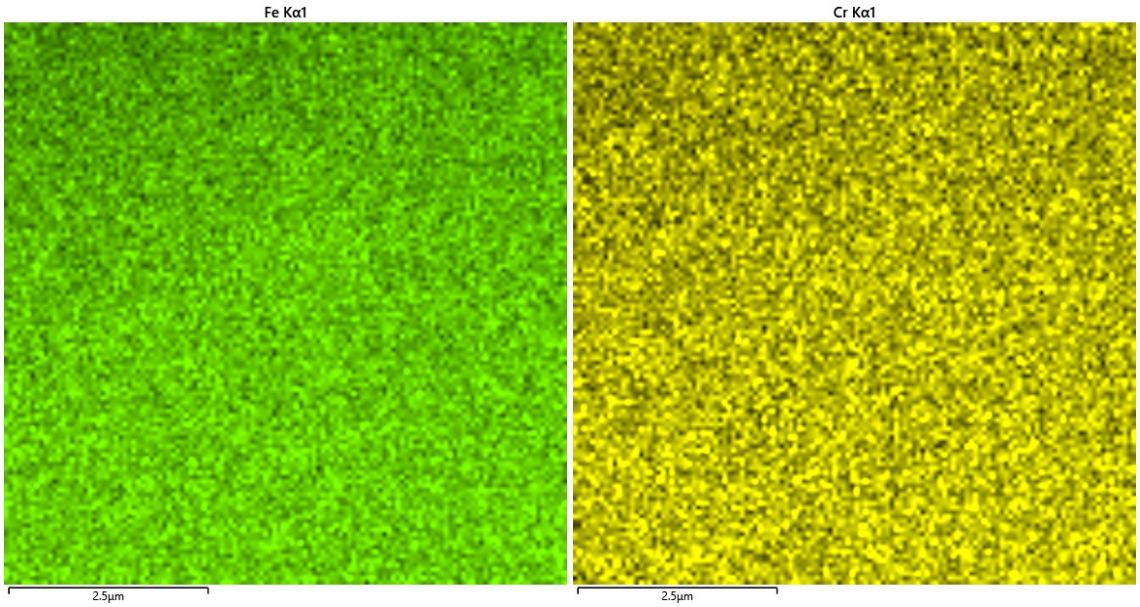

(f) Iron (Fe) (g) Chromium (Cr)

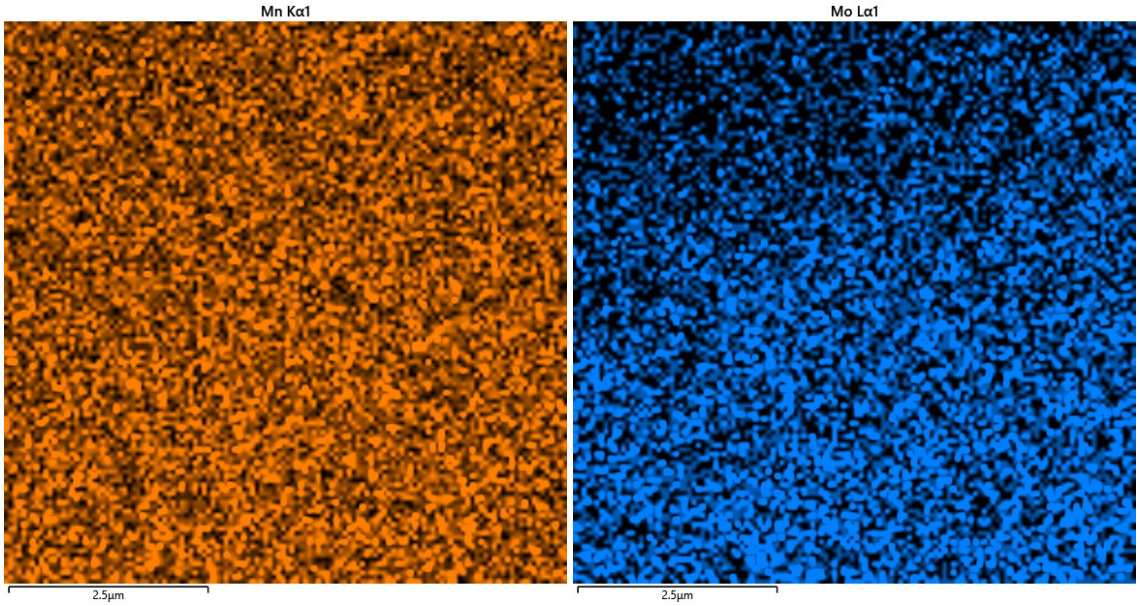

(h) Manganese (Mn) (i) Molybdenum (Mn)

Figure A.2 α spectrum of the chemical characteristics within the respective sample area

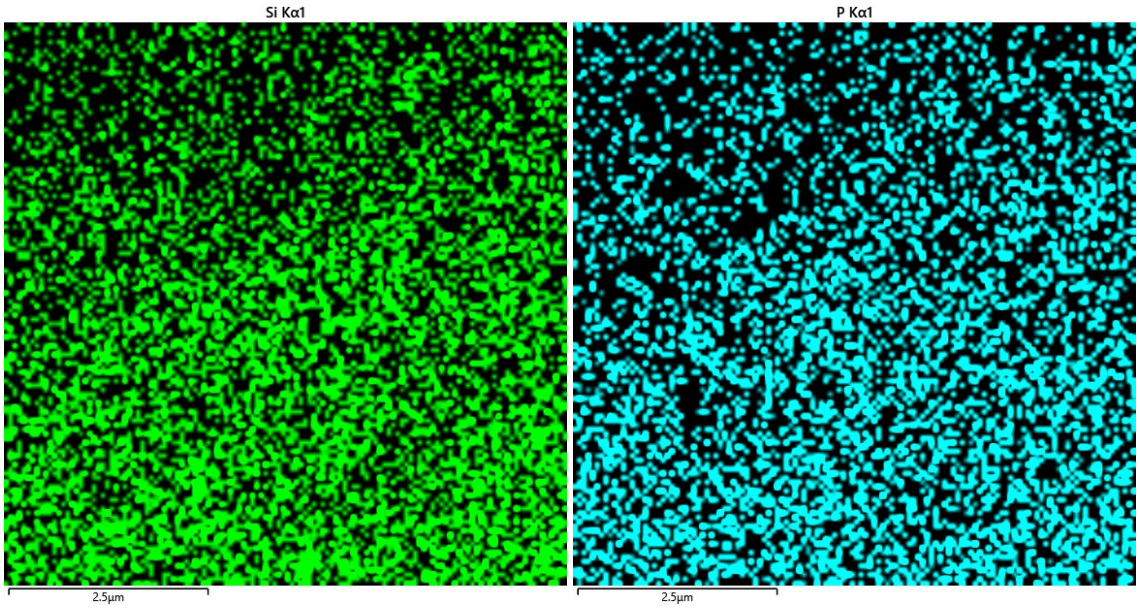

(j) Silicon (Si) (k) Phosphorous (P)

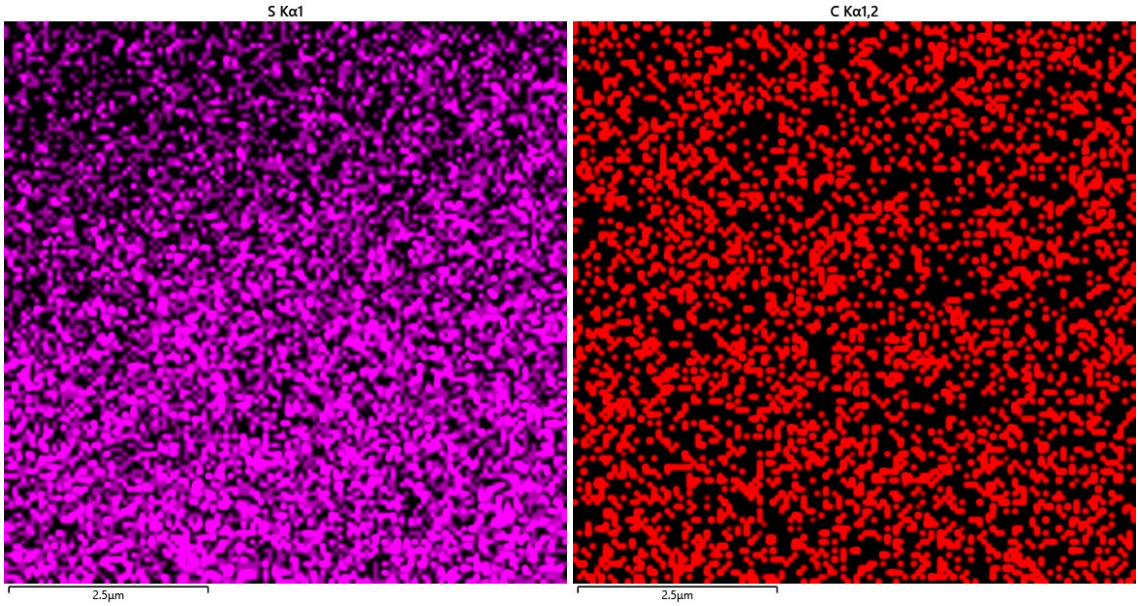

(l) Sulfur (S) (m) Carbon (C)

Figure A.3 α spectrum of the chemical characteristics for the rest of the compounds observed

APPENDIX B: TUNGSTEN PARTICLE TRACKING

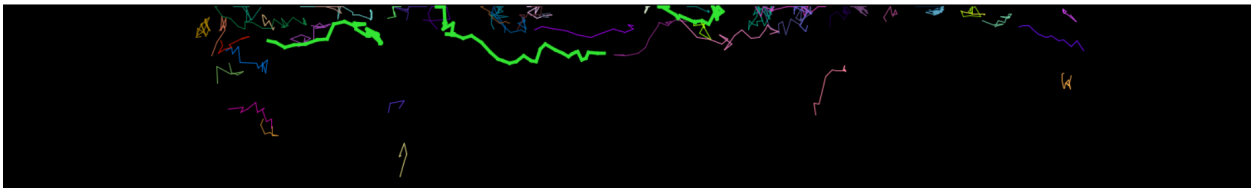

(n) EXP 189

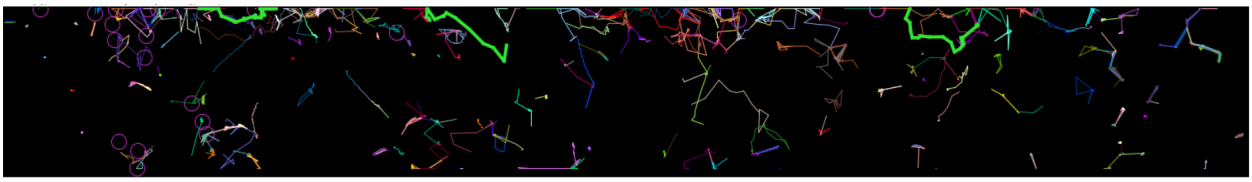

(o) EXP 173

Figure B.1 Tracks of particles in S1, S2, and S3 zones, denoted by the bight-green tracks